Novel Methods for Optically Measuring Whitecaps under Natural Wave-Breaking Conditions in the Southern Ocean

KAYLAN RANDOLPH, HEIDI M. DIERSSEN, AND ALEJANDRO CIFUENTES-LORENZEN

Department of Marine Sciences, University of Connecticut, Groton, Connecticut

WILLIAM M. BALCH

Bigelow Laboratory for Ocean Sciences, East Boothbay, Maine

EDWARD C. MONAHAN

Department of Marine Sciences, University of Connecticut, Groton, Connecticut

CHRISTOPHER J. ZAPPA

Lamont-Doherty Earth Observatory, Columbia University, Palisades, New York

DAVE T. DRAPEAU AND BRUCE BOWLER

Bigelow Laboratory for Ocean Sciences, East Boothbay, Maine

(Manuscript received 22 April 2016, in final form 28 November 2016)

ABSTRACT

Traditional methods for measuring whitecap coverage using digital video systems mounted to measure a large footprint can miss features that do not produce a high enough contrast to the background. Here, a method for accurately measuring the fractional coverage, intensity, and decay time of whitecaps using above-water radiometry is presented. The methodology was developed using data collected in the Southern Ocean under a wide range of wind and wave conditions. Whitecap quantities were obtained by employing a magnitude threshold based on the interquartile range of the radiance or reflectance signal from a single channel. Breaking intensity and decay time were produced from the integration of and the exponential fit to radiance or reflectance over the lifetime of the whitecap. When using the lowest magnitude threshold possible, radiometric fractional whitecap coverage retrievals were consistently higher than fractional coverage from high-resolution digital images, perhaps because the radiometer captures more of the decaying bubble plume area that is difficult to detect with photography. Radiometrically obtained whitecap measurements are presented in the context of concurrently measured meteorological (e.g., wind speed) and oceanographic (e.g., wave) data. The optimal fit of the radiometrically estimated whitecap coverage to the instantaneous wind speed, determined using robust linear least squares, showed a near-cubic dependence. Increasing the magnitude threshold for whitecap detection from 2 to 4 times the interquartile range produced a wind speed–whitecap relationship most comparable to the concurrently collected fractional coverage from digital imagery and previously published wind speed–whitecap parameterizations.

1. Introduction

Whitecaps on the ocean surface, formed by breaking waves, are features of significant importance to air–sea interaction. Whitecaps foster climate-relevant physical and chemical processes in the ocean, including the production of sea salt aerosols, mixing processes, and the exchange of gas (e.g., CO_2, CH_4, DMS, water vapor) and heat with the atmosphere. Efforts to parameterize these processes in climate models generally incorporate an estimate of fractional whitecap coverage (e.g., Monahan and Spillane 1984; Liss and Merlivat 1986; Asher et al. 2002; Fairall et al. 2003; Scanlon et al. 2016).

Corresponding author e-mail: Kaylan Randolph; kaylan.randolph@uconn.edu

DOI: 10.1175/JTECH-D-16-0086.1

Typically, whitecap coverage W is a combined measurement of both stages A and B, where stage A includes the active spilling crest and a dense, broad bubble size spectrum. Stage B is the maturing stage A whitecap, which covers a larger area and has a relatively narrow bubble spectrum (Monahan and Lu 1990). During stage A breaking, large volumes of air are introduced into the surface layer of the ocean (i.e., the α bubble plume) (Monahan and Lu 1990). Therefore, air–sea gas transfer velocities are often based on the fractional coverage of stage A whitecaps (Asher et al. 2002, 1995; Monahan 2002). The entrained air is fragmented during the stage A phase, and the resulting bubbles are distributed during the stage B phase (i.e., β plume). Bubble processes (dissolution, bursting, etc.) occur during and after this phase. The stage B bubble plume is largely responsible for the production of primary marine aerosols and can impact heat flux (Monahan et al. 1986; Andreas et al. 1995). Under moderate to high wind conditions ($>7\,\mathrm{m\,s^{-1}}$), whitecaps can support bubble populations in uniform, persistent (3–4 h) subsurface plumes [i.e., γ plumes in the usage of Monahan and Lu (1990)], which are relevant to the supersaturation of dissolved gases in the surface ocean (Thorpe 1982; Monahan 1993). Accurate, practicable techniques for quantifying the coverage and breaking intensity of whitecaps from initiation through decay are necessary to understand these processes.

As a result of advances in photographic and computing technology, methods for estimating whitecap coverage include the analysis of high-resolution digital images covering a large footprint (e.g., hundreds to thousands of square meters) obtained using camera systems positioned at an oblique angle approximately 15–20 m above the sea surface. Historically, imagery was processed manually using a simple ''threshold'' technique (e.g., Nordberg et al. 1971; Ross and Cardone 1974; Monahan et al. 1984), where a selected intensity value separates whitecaps from the background surface. This is done on an image-by-image or small batch basis because of fleeting changes in ambient illumination. To facilitate image processing, automated techniques that use an objective approach for threshold selection have been introduced (e.g., Sugihara et al. 2007; Callaghan and White 2009; Kleiss and Melville 2011). Hundreds of images are analyzed per 20-min sampling period to produce convergent coverage estimates (Callaghan and White 2009). At present, the automated whitecap extraction (AWE) algorithm, applied to images with a large footprint, is perhaps the most commonly applied method for estimating whitecap coverage (Callaghan and White 2009). However, AWE and other automated techniques require high-quality images free of sun glint and sky reflectance, and with homogeneous illumination that is often challenging to obtain in the field.

The viewing geometry of the digital camera systems configured to view large areas of the ocean surface allows for detection of only the near-surface very bright manifestations of the whitecap feature. Therefore, features that do not produce a sufficiently strong contrast to the background, including whitecaps small in size, thin patches of surface foam, and the submerged bubble plumes, are missed (Stramska and Petelski 2003; Callaghan and White 2009). Because foam and bubble entrainment from breaking waves has a pronounced effect on the magnitude of visible light leaving the ocean surface (e.g., Koepke 1984; Frouin et al. 1996; Moore et al. 2000; Stramski and Tegowski 2001; Terrill et al. 2001; Zhang et al. 2002), they are easily detected in measurements of optical radiance. Therefore, ocean color radiometers, highly sensitive to small changes in upwelling radiance, collecting at a fast sampling rate within a small area can be used to measure more of the elusive whitecap features.

A novel method for obtaining whitecap coverage and wave-breaking intensity using radiance measurements is presented here. The radiometric quantities measured, an estimate of the spatial coverage associated with the temporal, point-based measurement of whitecaps, and the configuration of the instruments are included in section 2. The development of the radiometric method for measuring whitecap quantities, including the removal of a baseline and statistical approach for identifying whitecap features in the record, is described in section 3. Data collected at several stations in the Atlantic sector of the Southern Ocean during a wide range of physical forcing and wave-breaking conditions are presented in section 4. An assessment of the method, including the removal of the baseline and a selection of whitecap records using single- and double-radiometer systems, is presented in section 5a. The whitecap quantities resolved are reported in the context of simultaneously collected meteorological and oceanographic measurements. The radiometerically estimated whitecap coverage was compared to coverage measured during the experiment using the digital imaging technique in section 5b. The wind speed–whitecap coverage relationship resulting from the use of the radiometric approach is compared to previously published, widely recognized parameterizations for consistency in section 5c. Sources of errors in the estimates of whitecap quantities resulting from the use of this method are discussed at the end of section 5. Finally, a summary of the advantages of using radiometers to measure whitecaps

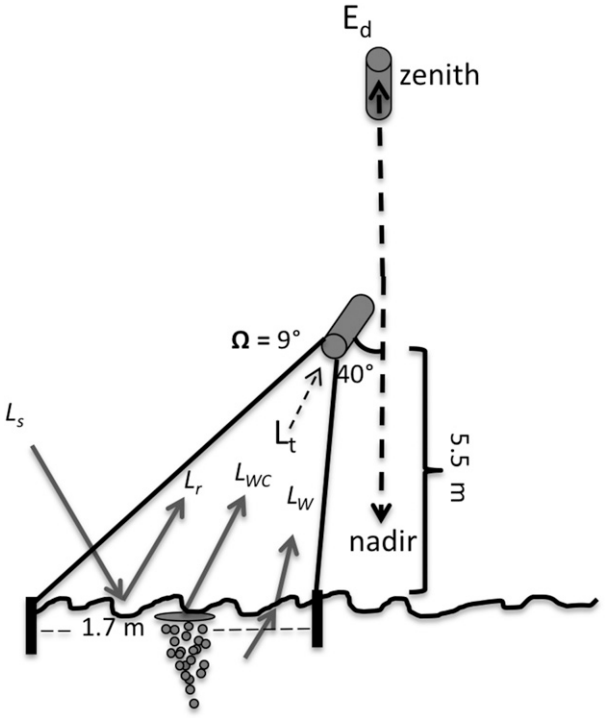

FIG. 1. Radiance from the surface ocean under windy conditions. The total measured upwelling radiance $L_t(\theta, \varphi)$ includes the water column component $L_w(\theta, \varphi)$, the whitecap component $L_{\mathrm{WC}}(\theta, \varphi)$, and the surface-reflected portion $L_r(\theta, \varphi)$ of the incident sky radiance $L_s(\theta', \varphi')$.

and recommendations for improving upon the method are presented in section 6.

2. Radiometric measurements of whitecaps

a. Principle of radiometric measurements

Whitecap radiance is not directly measureable, but it can be inferred from the total upwelling radiance signal measured above the sea surface. Upwelling radiance from the surface ocean is dependent on the water optical properties, the geometric structure of the incident radiance distribution (i.e., solar zenith angle), the geometry of the surface, and the illumination conditions (e.g., cloud cover). It is a directional quantity measured over time, area, solid angle, and wavelength interval (Mobley 1999). Here, the total upwelling radiance signal above the sea surface, $L_t(\theta,\varphi,\lambda)$, is the spectral distribution of light, or radiant power2 per unit area, wavelength and solid angle ($\mathrm{W\,m^{-2}\,nm^{-1}\,sr^{-1}}$), emerging from the ocean in polar and azimuthal directions θ and φ, respectively,

$$L_t(\theta,\phi,\lambda), = L_w(\theta,\phi,\lambda) + L_r(\theta,\phi,\lambda) + L_{\mathrm{WC}}(\theta,\phi,\lambda), \quad (1)$$

where L_w is the radiance signal of the undisturbed water column, L_{WC} is the radiance signal from whitecaps (i.e., foam and bubbles), and L_r is the surface-reflected portion of the incident sky radiance L_s (Fig. 1). The magnitude of L_r is dependent on the solar zenith angle, viewing geometry, the wavy surface, and the sky conditions. The total contribution of breaking waves to radiance can be captured at a high sampling rate above the sea surface using a multispectral or single-channel radiometer (details in section 4).

b. Temporal point-based versus spatial measurements of whitecaps

Typically, hundreds of digital images with a large footprint are required per 20-min record length to accurately estimate fractional whitecap coverage due to the intermittent and nonuniform nature of wave breaking (Callaghan and White 2009). There are trade-offs between producing coverage estimates that are stable (i.e., converging, by increasing the dataset size) and also representative of the forcing conditions. Ideally, the size of a large footprint would be optimized so that background pixel intensities, which include the influence of sky reflectance, are statistically uniform, and variability from heterogeneous sky conditions and viewing geometry are minimized. Small footprints require a large number of images to be used in retrieving accurate coverage estimates. Collecting many measurements of an $\sim 1\,\mathrm{m}^2$ instantaneous field of view (IFOV), a measure of the spatial resolution of a remote sensing system, at a high sampling rate is an alternative to capturing a large area at any instant (e.g., Wang et al. 1995; Moore et al. 1998). A comparison between cameras measuring whitecap coverage within a larger footprint and a microwave radiometer/camera system measuring a small ($\sim 1\,\mathrm{m}^2$) footprint over time produced consistent results, substantiating the use of measurements of very small areas at a high sampling rate over time for accurately predicting spatially averaged whitecap coverage (Wang et al. 1995). Similarly, Moore et al. (1998, 2000) reported the coverage of thick (active) to thin (residual) foam patches by taking many reflectance measurements (7-Hz sampling rate) of a small area on the water surface (~14-cm-diameter circle).

When measuring a small area, the longer the record length, the better the statistical base for obtaining one whitecap coverage estimate (i.e., W data point); however, the associated meteorological and oceanographic conditions can change on relatively short time scales. The wrong record length choice could introduce biases and aliasing into coverage estimates as a result of different sea states (e.g., wave height and period) and types

of breaking (e.g., spilling and plunging breakers). For example, in developed seas, breaking occurs less frequently (e.g., Gemmrich and Farmer 1999; Gemmrich et al. 2008), but it can be at a higher intensity (e.g., deeper bubble penetration depths relative to younger seas); significant wave height has been used to scale the enhancement in the subsurface turbulent kinetic energy dissipation rate associated with wave breaking (e.g., Terray et al. 1996; Drennan et al. 1996). Under these conditions a longer time series is required to sample accurately compared to developing seas, where breaking occurs more frequently. When a generic record length is required, it should be decided based on the lowest frequency of breaking to be resolved.

Our method proposes obtaining the spatial average of whitecap coverage by collecting a continuous time series of radiance measurements at high sampling frequency within a small area (e.g., $\sim 1\,\mathrm{m}^2$). Several steps were taken in an effort to constrain the record length necessary and to ensure statistical robustness. The spatial coverage or footprint A (m^2) of the point-based sampling approach is a function of the diameter of the IFOV D, the record length Δt, and an estimate of the surface drift velocity u_s (a function of the wind stress and speed over ground on a moving vessel),

$$A(D, t, u_s) \sim D(u_o + u_{\mathrm{SOG}})\Delta t. \tag{2}$$

Radiance measurements are considered stationary, while the ship maintained a constant heading into the wind and speed over ground SOG of less than $1\,\mathrm{m\,s^{-1}}$. Under these conditions, the surface drift velocity associated with ship motion u_{SOG} is close to zero. Therefore, the surface drift velocity is assumed to be the advection velocity associated with a passing whitecap (u_o) only and was approximated following Wu (1983):

$$u_o = \alpha u_*, \tag{3}$$

where u_* ($\mathrm{m\,s^{-1}}$) is the atmospheric friction velocity and α is a numerical constant ($\alpha = 0.53$).

The observed whitecap coverage can be compared to an independently estimated whitecap coverage and the expected number of events for consistency. For a specified footprint and surface drift velocity, the whitecap coverage a over the time interval Δt is given by

$$a(\Delta t) = A w_c, \tag{4}$$

where w_c is an estimate of the whitecap coverage given the physical or meteorological conditions (i.e., the wind speed at 10 m U_{10}; $\mathrm{m\,s^{-1}}$). Using this relationship and the experimental data of Bondur and Sharkov (1982) describing the area (m^2) of individual whitecaps a_{wc}, the number of independent events within the time interval $N(\Delta t)$ can be estimated as

$$N(\Delta t) = \frac{a(\Delta t)}{a_{\mathrm{WC}}}. \tag{5}$$

Events resolved using the radiometric method were considered independent when spaced by 30 s or more. The equivalent minimum areal coverage necessary to obtain a statically robust measurement of whitecap coverage using the point-based approach was determined by minimizing the variance in whitecap coverage measured during sustained physical forcing conditions and by comparison with coverage measured using digital imagery.

The final consideration is the surface renewal time, the rate of encounter with a whitecap event, and the sampling rate. The surface renewal time t_r (s) is the ratio of the diameter of the IFOV to the surface drift velocity,

$$t_r = D/u_o. \tag{6}$$

For example, for a surface drift velocity of $0.3\,\mathrm{m\,s^{-1}}$ the surface renewal time is 3.3 s (0.30 Hz). An instrument with a sampling rate of 7 Hz (typical for the radiometer systems described here) with a Nyquist frequency of 3.5 Hz and a signal-to-noise ratio of 2–2.5 Hz can be used to resolve features with a maximum surface drift velocity of $2\,\mathrm{m\,s^{-1}}$. These conditions could allow for underway sampling.

3. Method for extracting whitecap quantities

The time series of radiometric measurements are first analyzed to identify whitecap events. Whitecap realizations within the time series are used to estimate wave-breaking quantities, namely, whitecap coverage, optical intensity, duration, and decay time.

a. Identifying whitecap events

Whitecap events are identified in the radiometric time series following the basic procedure outlined in Fig. 2, for two possible radiometer configurations. For a single-radiometer system, whitecap features are obtained from the total radiance signal L_t [Eq. (2)]. A nonstationary L_t signal, producing mean and variance values that change over time, can arise from unpredictable fluctuations or trends in the illumination conditions or changes in L_w (e.g., the color of the water column without bubbles or foam). A stationary

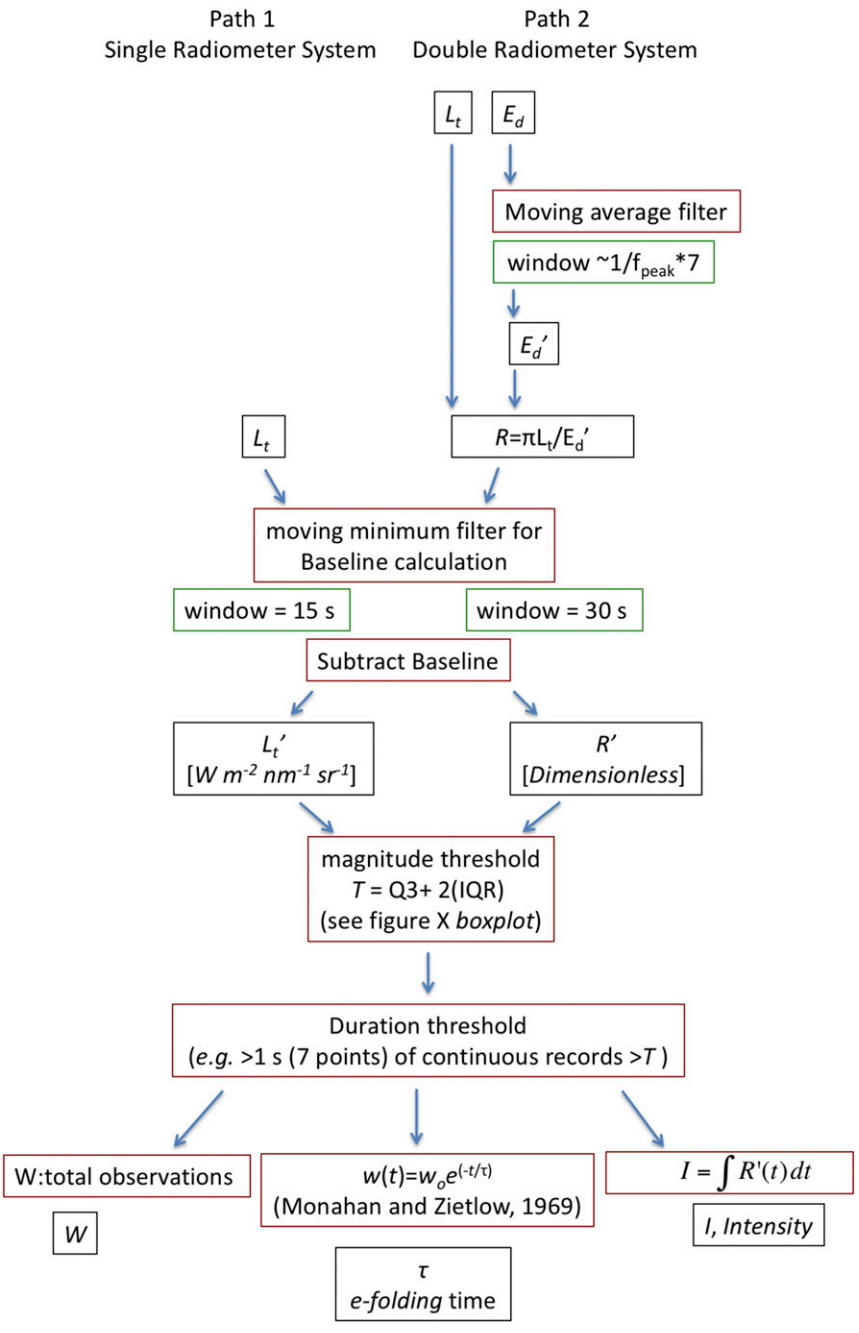

FIG. 2. Procedure for retrieving whitecap quantities (i.e., coverage, decay time, and optical intensity) from measurements of radiance L_t (path 1) and irradiance E_d (optional; path 2).

upwelling radiance time series L' can be estimated from the measured nonstationary L_t signal by applying a moving minimum–maximum (min–max) filter (e.g., Briggs et al. 2011 following Lemire 2006). Ideally, the baseline captures all changes in illumination conditions, eliminating the need for normalizing L_t to the measured downwelling irradiance at each time step. The baseline also accounts for magnitude differences in L_t between stations due to spectral changes in the water color itself or L_w. The moving min–max filter simultaneously finds the minimum and maximum elements within a sliding time window of a specified length. The window length is optimized such that the time interval is short enough to remove variations in radiance due to changing illumination conditions, while it is long enough not to erode whitecap

features. At a minimum, the window length should be at least the length of the longest whitecap feature (e.g., ~40 s). During uniform sky conditions, L_t is stationary over the time interval necessary to capture whitecap quantities and long window lengths are realistic. However, nonuniform skies require shorter window lengths for L_t to approach a stationary condition and potential errors can arise in identifying the limits of the whitecap feature. Here, a single optimized window length of 15 s was used for all data. However, window lengths can be easily varied based on the prevailing illumination conditions.

A double-radiometer system is required for highly variable sky conditions. In this case, identification of the whitecap feature can be detected more accurately if downwelling irradiance (E_d; $\mathrm{W\,m^{-2}\,nm^{-1}}$) is measured simultaneously with upwelling radiance. This approach requires the deployment of a second, upward-looking radiometer outfitted with a cosine collector, to measure the downward plane irradiance incident on the sea surface (see Fig. 2, path 2). In theory, the radiance reflectance term R ($\mathrm{sr^{-1}}$), which is the ratio of $L_t(t)$ to $E_d(t)$, accounts for changes in the illumination conditions and produces a stable measurement of the water and whitecaps. Assuming the measured L_t (θ, φ) is the same across all viewing directions (θ and φ), a Lambertian equivalent reflectance (LER) can be estimated by multiplying by π and the measurement becomes similar to a dimensionless albedo R' (Fig. 2). The E_d sensor must be deployed in a location where it is unaffected by ship shadow, typically high up on the jack staff of a ship (Zibordi and Donlon 2014). It is difficult to gimbal the instrument so that it remains plane parallel when deployed on a moving platform. For the Southern Ocean, the instrument oscillated between nadir (0°) and ~3° to 5° in any direction (Cifuentes-Lorenzen et al. 2013).

Slight changes in the look angle of the sensor due to ship motion can produce regular fluctuations in the E_d signal at approximately the period of the swell (e.g., ~10 s). Therefore, before calculating R', the E_d data can be filtered using a moving average, where the window length is at least as long as the swell period. Here, the peak period of motion-induced fluctuations, determined from the average power spectral density (PSD) of E_d (~1-min segments), was used as the window length for the moving average filter. This automated and objective filtering approach removes low-magnitude variance as a result of the changing look angle, but it maintains trends in R' for use in the calculation of whitecap features following the same baseline removal process described above.

With the baseline removed, the L' or R' record (see Fig. 2) has a distribution that is positively skewed to a degree dependent on the presence of bright foam, bubbles (e.g., the more whitecaps, the heavier the tail), and glint. Glint acts as a signal contaminant and appears randomly as bright features, lasting <2 s in duration. The width of the L' or LER$'$ distribution (variance, σ^2) is dependent on skylight reflected off of the wavy surface (L_r), another signal contaminant. The frequency and magnitude of variance in the upwelling radiance signal is the result of time-varying features of the different types of waves, including gravity waves on the order of meters in length to capillary waves on the order of millimeters in length, at each time step. The greater the surface-reflected skylight, the larger the variance in the background signal and the more difficult identifying whitecaps becomes, especially in the case of low-intensity breaking (i.e., spilling waves).

Whitecaps can be identified in the L_t' or R' record using a number of different methods depending on the needs of the user. Here, a station-specific threshold was determined using a single objective approach that is robust to outliers. The interquartile range (IQR) of L' or R' was calculated as the difference between the 75th (Q3) and 25th (Q1) percentiles. The magnitude of the IQR is dependent on the surface-reflected skylight, which is, in turn, dependent on the wave and illumination conditions. Uniform skies and a flat ocean yield low IQR, and variable skies and a roughened sea surface yield high IQR. Outliers (or breaking waves) are defined as samples greater than Q3 + 2(IQR). For normally distributed data, whisker lengths are typically set to 1.5(IQR), which corresponds to 2.7σ. After the threshold has been applied, any remaining nonwhitecap, transient bright features (e.g., glint) are removed from the signal using a despiking procedure based on feature duration. Any bright features lasting <2 s are considered glint features and deemed nonwhitecap.

b. *Estimating wave-breaking and whitecap quantities*

Fractional whitecap coverage can be calculated as the fraction of the total record that was identified as a whitecap feature. The record length for producing statistically robust fractional whitecap coverage estimates must be considered. If the record length is too short, the variance will be too high to produce stable whitecap quantities. In theory, under strong forcing conditions with whitecap coverage on the order of 10^{-2}, 10 whitecap realizations are obtained per every 1000 points recorded, which corresponds to ~140 s. For low-coverage days (e.g., W of ~0.001), 10 points of whitecap realizations are identified per every 10 000 points recorded, which

corresponds to a ~1400-s or 23-min record. For comparison purposes, 20-min segment lengths, which can resolve fractional coverage on the order of (10^{-4}), are commonly reported when using digital imaging techniques. In reality, whitecaps are nonuniform in space and time, and the frequency breaking is strongly dependent on the forcing conditions (see section 2b). A sensitivity analysis illustrating the space-to-time relationship is presented below based on the Southern Ocean data. Finally, the relationship between neutral wind speeds at 10 m and radiometrically obtained whitecap coverage estimates was investigated using ordinary least squares and compared to previously published wind speed–whitecap parameterizations (e.g., Monahan and Muirchaertaigh 1980; Stramska and Petelski 2003).

The radiometric approach also allows for the estimation of other whitecap quantities beyond fractional coverage. For example, a whitecap decay time τ can be obtained from R' estimated for individual whitecap events considered to be complete. Following Monahan and Zietlow (1969), τ is calculated as the exponential fit from the L' or R' measured at the initial time of the peak t_0 to the final whitecap realization t_f, where t is ($t_f - t_0$) following

$$\mathrm{LER}'(t_f) = \mathrm{LER}'(t_0)e^{-t/\tau}.$$

The duration and maximum brightness of each measured whitecap was used to identify full or near-full events (rather than partial events) for calculating decay time and breaking intensity. When applied to the upper 75th percentile in duration and brightness, the *e*-folding times produced using the radiometric method were found to be comparable to those published in the literature (e.g., ~3.5 to 4.5 s).

The measured radiance can also be integrated over the lifetime of the whitecap to provide an indicator of the magnitude of the whitecap event. This term, defined here as the whitecap reflectivity factor, physically related to the breaking intensity I, can be estimated from the L' *or* R' measurements from the start of the feature t_i to the end of the feature t_f following

$$I = \int_{t_i}^{t_f} R'(t)\,dt,$$

where t_i and t_f are the first and last data points in a continuous set of points exceeding the specified IQR-based threshold.

4. Measurements

The methodology presented here was evaluated using data collected as a part of the Southern Ocean Gas Exchange Experiment (SO GasEx) conducted on the NOAA ship the R/V *Ronald H. Brown* in the Atlantic sector of the Southern Ocean (50°S, 40°W) from 7 March to 4 April 2008. The primary objective of SO GasEx was to measure gas transfer at high wind speeds and to identify predictors, in addition to wind, for estimating gas transfer (Ho et al. 2011). Bubbles generated by breaking waves were measured as a part of this study (Randolph et al. 2014). A Lagrangian approach was taken to study relevant physical, chemical, and biological processes.

Two tracer patches were deployed lasting 6 and 15 days in duration, respectively. Measurements were collected at stations primarily north of South Georgia Island at a latitude of 51°S in a region characterized by moderate phytoplankton biomass and prone to high wind conditions, as shown in the satellite-derived average QuikSCAT wind speed imagery for March 2008 (Fig. 3). During yeardays 75–77, the sampling stations were located approximately 300 km farther south at a latitude of 54°S in waters surrounding South Georgia Island.

a. Instruments and configuration

A single-channel radiometer at visible wavelengths (here 411 nm) is sufficient to capture the full whitecap feature (e.g., stage A through the decaying bubble plume). The radiometer is configured to collect data over an azimuthal range of 270° across the heading of the ship while the solar zenith angle is above 20°. Sun glint and shadowing effects are minimized by maintaining a viewing direction 120° from the sun's azimuth. A viewing angle of 40° from nadir is employed to minimize specular reflectance of the sun's direct beam into the detector (Mueller et al. 2003). Proper viewing angles can be maintained using a computer-based system that calculates the sun's azimuth angle relative to the ship and adjusts the position of the detector using a stepping motor (see Balch et al. 2011). An integrated dynamic positioning system for radiometers is now commercially available (e.g., Satlantic, Sea-Bird Scientific).

The down-looking radiometer is positioned above the water surface to maintain an ~1-m^2 instantaneous field of view. In the open ocean, the spatial coverage condition is satisfied for record lengths of 20–40 min or more, depending on the drift velocity and the number of events observed under those conditions. While a calibrated, dark corrected signal is preferred if making quantitative comparisons of intensity and duration of whitecaps between regions, the data are normalized to a baseline, which removes most of the calibration artifacts and whitecaps are evaluated as

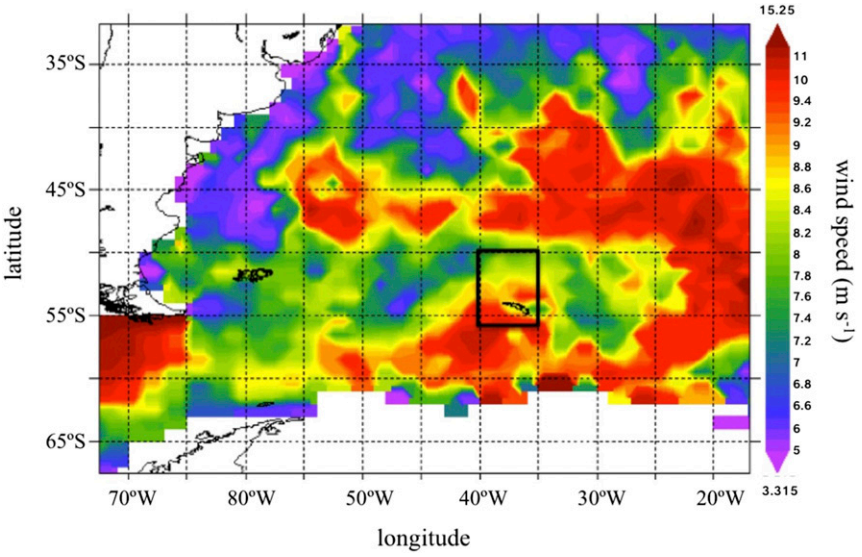

FIG. 3. The South Atlantic sampling region with the mean monthly QuikSCAT-estimated wind speed ($m\,s^{-1}$) for the month of March and the SOGasEx sampling location (black box) from NASA JPL.

relative enhancements to the radiance signal. Under shifting sky conditions, it is not necessary but advantageous to have simultaneously collected E_d measurement to normalize the radiance to the incident irradiance.

The radiometric data were collected as a 0.5- ~2.5-h time series while on station and from 1100 to 1600 UTC, during which the ship maintained a constant heading. Three radiometric sensors were deployed, including a downwelling irradiance sensor mounted at 18 m on the jack staff of the ship to avoid ship shadow, and down-looking and sky-viewing radiance sensors, each with seven channels between 412 and 680 nm (10-nm spectral bandwidth) (Fig. 4). The downwelling irradiance and sky-viewing radiance signals were collected to aid in the development of the method but are not essential for its implementation. The radiance sensors have a 6° field of view (FOV) and were deployed from the bow of the ship ~8 m above the water surface, resulting in an ~1-m^2 instantaneous field of view. Radiometric data were processed to produce calibrated and dark current corrected data interpolated onto common time coordinates.

b. Ancillary data

In addition to radiometric measurements, whitecap coverage was estimated using high-resolution digital images from two Imperx charge-coupled device (CCD) cameras sampling 100-m^2 areas with approximately 4-cm resolution at 5 Hz from the Flying Bridge (port and starboard side looking) of the R/V *Ronald H. Brown* (Zappa et al. 2012) (Fig. 5). Lens distortion effects were removed following Bouguet (2004) and a motion correction (i.e., pitch, roll, and yaw) was applied using the inertial motion unit–measured angular rates. Background intensity gradients were removed and whitecaps were identified using the approach of Callaghan and White (2009).

Measurements of turbulent wind velocity fluctuations, wind speed and direction, relative humidity, and air temperature were collected at 18 m using a direct covariance flux package (Edson et al. 2011). Heat fluxes (sensible and latent) and long-wave (IR) radiative flux were estimated based on the COARE algorithm (Fairall et al. 2003). Neutral wind speeds at the reference height of 10 m (U_{10N}) were obtained by accounting for stability based on the Monin–Obukhov similarity theory (Edson and Fairall 1998). The wave frequency spectrum from 0.03 to 1.2 Hz was determined by combining measurements from an X-band radar [Wave Monitoring System II (WaMoS II)], a laser altimeter (Riegl LD-90), and a microwave unit [Tsurumi-Seiki America, Inc. (TSKA) shipborne wave height meter (SWHM)] (Cifuentes-Lorenzen et al. 2013). Wave field statistics, including the significant wave height of the dominant waves H_s and the phase speed at the spectral peak c_p were determined from the measured wave frequency spectrum. Inverse wave age (U_{10}/c_p) was also derived from the measured wavenumber and frequency spectra to describe the state of the wind-wave field. For open ocean conditions, high inverse wave age values (i.e.,

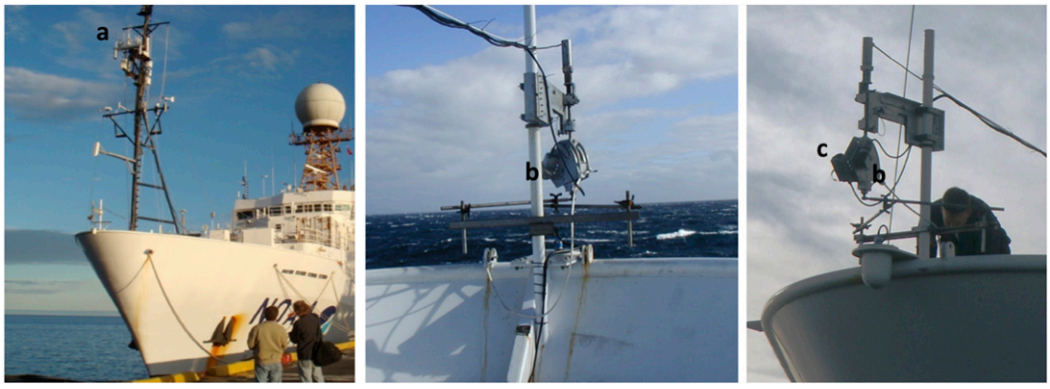

FIG. 4. The three radiometric sensors deployed during SO GasEx: (a) a downwelling irradiance sensor mounted on the top of the jack staff at 18 m, and (b) down-looking and (c) sky-viewing radiance sensors deployed at the bow. The downwelling irradiance and sky radiance signals are used as ancillary data and are not required in retrieving whitecap quantities. Proper viewing angles were maintained using a computer-based system that calculated the sun's azimuth angle relative to the ship and adjusted the position of the detectors using a stepping motor. A new version of this design is now available commercially (Sea-Bird/Satlantic).

$U_{10}/c_p > 0.82$) are considered young or developing seas, while low values (i.e., $U_{10}/c_p < 0.82$) are considered old or developed seas. The threshold, $U_{10}/c_p \sim 0.82$, is considered mature or fully developed (Kudryavtsev and Makin 2002).

During SO GasEx, the wind speed ranged from 4 to 20 m s^{-1}, the seas were mostly developed, and the atmospheric stability was near neutral (Fig. 6). Whitecap coverage measured using digital imagery ranged from 0% to 6% (Fig. 6, black circles). Radiometric data collected on 18 of the total 35 days of the experiment (U_{10N} ~4–15 m s^{-1}) were used to develop this method (Table 1; Fig. 6, box). Wind and wave data were used to investigate deviations of the radiance-derived whitecap coverage from the published wind speed–whitecap parameterizations (e.g., Monahan and Muircheartaigh 1980; Monahan 1993; Asher and Wanninkhof 1998; Hanson and Phillips 1999; Stramska and Petelski 2003; Villarino et al. 2003).

5. Assessment of the method

The large range in meteorological, sea, and sky conditions (e.g., state of the wave field, wind speed, and cloud cover) measured during SO GasEx make the dataset ideal for assessing the robustness of the methodology presented here and in identifying its limitations. Here, potential sources of error using the path 1 and 2 approaches for obtaining whitecap quantities are addressed and recommendations for their application are made (section 5a). A comparison between radiometrically estimated coverage and coverage determined using digital imagery and the Callaghan and White (2009) AWE technique is presented. Radiometrically estimated whitecap measurements are presented in the context of concurrently measured meteorological and oceanographic data (section 5b). Finally, the dependence of the whitecap coverage estimated here on wind speed is explored using robust least squares fitting, and the resulting relationship is compared to previously published and widely accepted wind speed–whitecap parameterizations section 5c).

a. Results on the methodology

Over 35 h of radiometric data collected while on station in the Southern Ocean was used to assess the whitecap retrieval methodology presented here. Results from the use of a single sensor (i.e., path 1), which makes for a simple deployment and eliminates the need for two intercalibrated radiometers, are presented. Under most sea and sky conditions encountered in this study, the baseline removal provided an effective means of accounting for both changing illumination conditions and water column optical properties.

Three L_t records collected under low (~4 m s^{-1}), moderate (~7 m s^{-1}), and high (14 m s^{-1}) wind speed conditions illustrate the strengths and limitations of following the path 1 approach (Fig. 7). The left-side panels of Fig. 7 show the raw upwelling radiance signal (L_t, black circles) and the baseline or moving min-max filtered L_t (gray circles). The right-side panels of Fig. 7 show the L' signal, resulting from the removal of the baseline from L_t (black circles). While on station, variation in L_w within the 15-s interval was negligible and

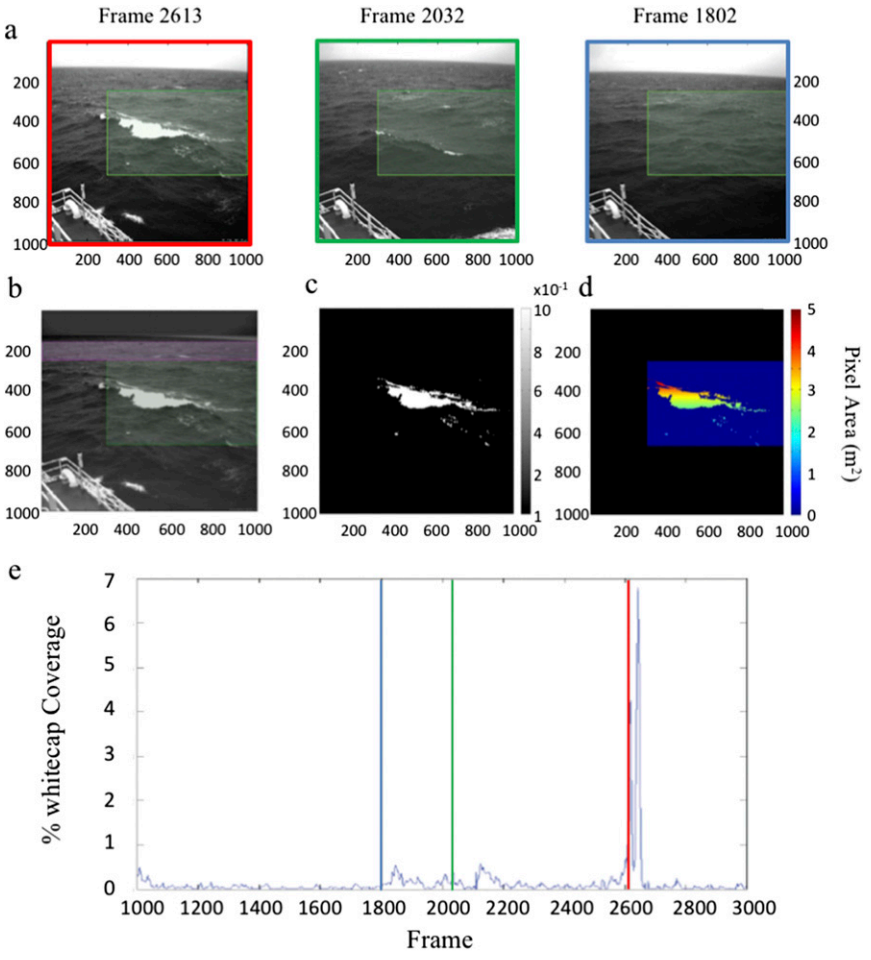

FIG. 5. (a) High-resolution digital imagery of whitecaps in the Southern Ocean collected using Imperx video cameras sampling 100 m^2 at 5 Hz (Zappa et al. 2012). The (b) background intensity gradients were (c) removed and a threshold was applied to identify pixels containing foam. (e) Whitecap coverage was estimated using (d) the whitecap pixel area for the three frames in (a) following the approach of Callaghan and White (2009).

was accounted for in the path 1 baseline removal. While the path 1 approach was effective at capturing breaking events lasting 15 s or less in duration (e.g., Figs. 7b, e), high intensity breaking (e.g., Figs. 7c,f) was better characterized and quantified following the path 2 approach.

For whitecap events lasting longer than 15 s, local minima occur within the event itself (Fig. 7c inset, gray dots); therefore, a portion of the whitecap feature was removed with the baseline (Fig. 7f). Small window lengths did not impact the whitecap coverage because the foam features remained well above the magnitude threshold, but they appeared less bright, resulting in an underestimation of optical intensity.

In the path 2 approach, E_d is used to account for changing illumination conditions. Large fluctuations in E_d produce a sharp trend in the L_t signal and the moving min–max filter underestimates the baseline (Fig. 7a inset, gray line), resulting in an overestimation of L' (Fig. 7d inset, black line). While the moving min–max filter was not optimal for use during nonuniform sky conditions (e.g., days 86 and 76 in Fig. 8), the slight overestimation in L' during day 86 did not result in an overestimation of W because the affected samples remained below the lowest magnitude threshold and so were not selected as whitecaps. Also, under nonuniform or clear-sky conditions (true for three SO GasEx stations, including days 75, 76, and 94), low-magnitude fluctuations in a nongimbaled E_d instrument occurred due to slight changes in the look angle (i.e., ~3°–5° in any direction) from ship motion (Fig. 8). The small motion-induced fluctuations in E_d resulted in large variance noise in R, and the E_d data were

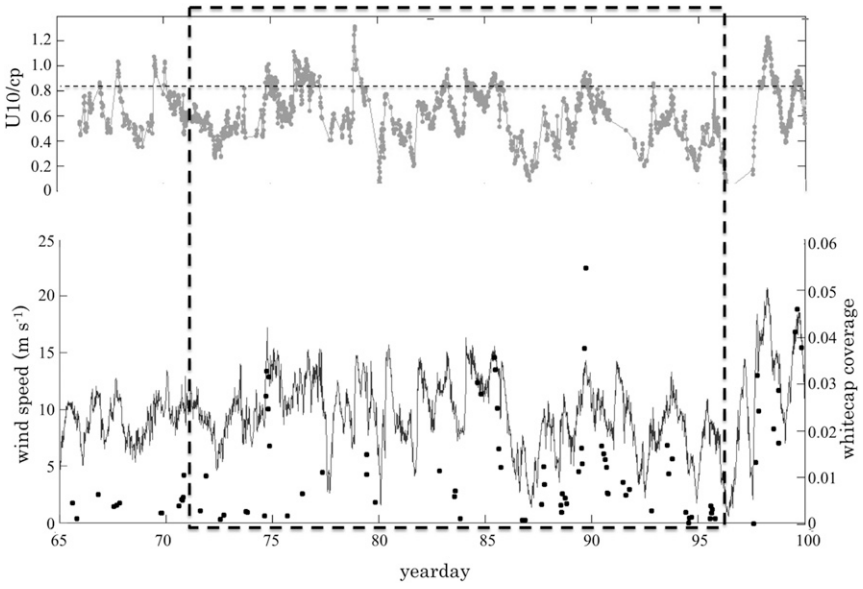

FIG. 6. The SO GasEx conducted in the Atlantic sector of the Southern Ocean (50°S, 40°W), 7 Mar–4 Apr 2008. (top) Measurements of the inverse wave age suggest that seas were mostly developed ($U_{10}/c_p < 0.82$) and under near-neutral conditions. (bottom) The wind speed ranged from 4 to 20 m s^{-1} (black line). Whitecap coverage measured using digital imagery ranged from 0% to 6% (black circles). Of the record 18 days were used to develop this method (dashed box).

filtered using a moving average based on the maximum time extent, and therefore the window length, of the peak in the E_d frequency spectrum (Fig. 9).

The path 2 approach was used to detect and evaluate the long (~35 s) whitecap events observed during day 76. Whitecap quantities were calculated for 20-min segments of radiometric data (8400 samples). The E_d signal was filtered using a moving average with a window length of 14 s (Fig. 10). The ratio of the raw L_t data to the moving-average filtered E_d data produced the reflectance term R. Application of the running min–max filter with a window length of 35 s to the R signal resulted in a baseline that did not erroneously include a portion of the whitecap feature, unlike when the min–max filter with a 15-s window was applied to L (Figs. 10a,b, pluses). The moving minimum approach offered only a low-resolution approximation of the ambient illumination conditions, whereas the high-resolution measurement of E_d was used in the calculation of R'; therefore the shapes of the L' and R' signals were similar but not identical (Fig. 10, example indicated with stars).

TABLE 1. A summary of the fractional whitecap coverage estimates in wind speed increments of 2 m s^{-1} from the digital imaging approach (W_D) and radiometric (W_R) approach using the 2(IQR) threshold. The difference between the mean whitecap coverage estimates for each bin from the two techniques is reported [$d_{2(\mathrm{IQR})}$], and the mean values were compared using a left-tailed t test assuming unequal variances. When the two means were determined to be statistically significantly different ($\alpha = 0.05$), the p values were reported. Other oceanographic measurements, including the significant wave height H_s, inverse wave age (U_{10}/c_p, where c_p is the peak phase speed in m s^{-1}), and the range in atmospheric stability ($\Delta T = T_{\mathrm{air}} - T_{\mathrm{water}}$), are presented to offer context for the W results.

Wind speed range (m s^{-1})	n	W_R [ste]	W_D [ste]	$d_{2(\mathrm{IQR})}$[a] (factor)	p value ($\alpha = 0.05$)	H_s (m)	U_{10}/c_p (range)	ΔT (°) (range)
4–6	3	0.0019 [0.0011]	0.0012 [0.0004]	1.6		7.2	0.29–0.43	−0.13–0.99
6–8	3	0.0092 [0.0026]	0.0016 [0.0004]	5.8	0	12.4	0.36–0.63	0.01–1.95
8–10	17	0.0150 [0.0012]	0.0054 [0.0007]	2.8	0	13.4	0.38–0.64	−3.05–2.38
10–12	6	0.0194 [0.0029]	0.0087 [0.0010]	2.2	2.0×10^{-4}	13.4	0.42–0.72	−0.47–2.61
12–14	11	0.0315 [0.0026]	0.0202 [0.0027]	1.6	1.7×10^{-2}	5.14	0.68–0.97	−2.41–3.16
>14	3	0.0546 [0.007]	0.0337 [0.0042]	1.6	2.4×10^{-2}	7.7	0.97–1.05	1.37–1.57

[a] Factor of 2.6 difference on average.

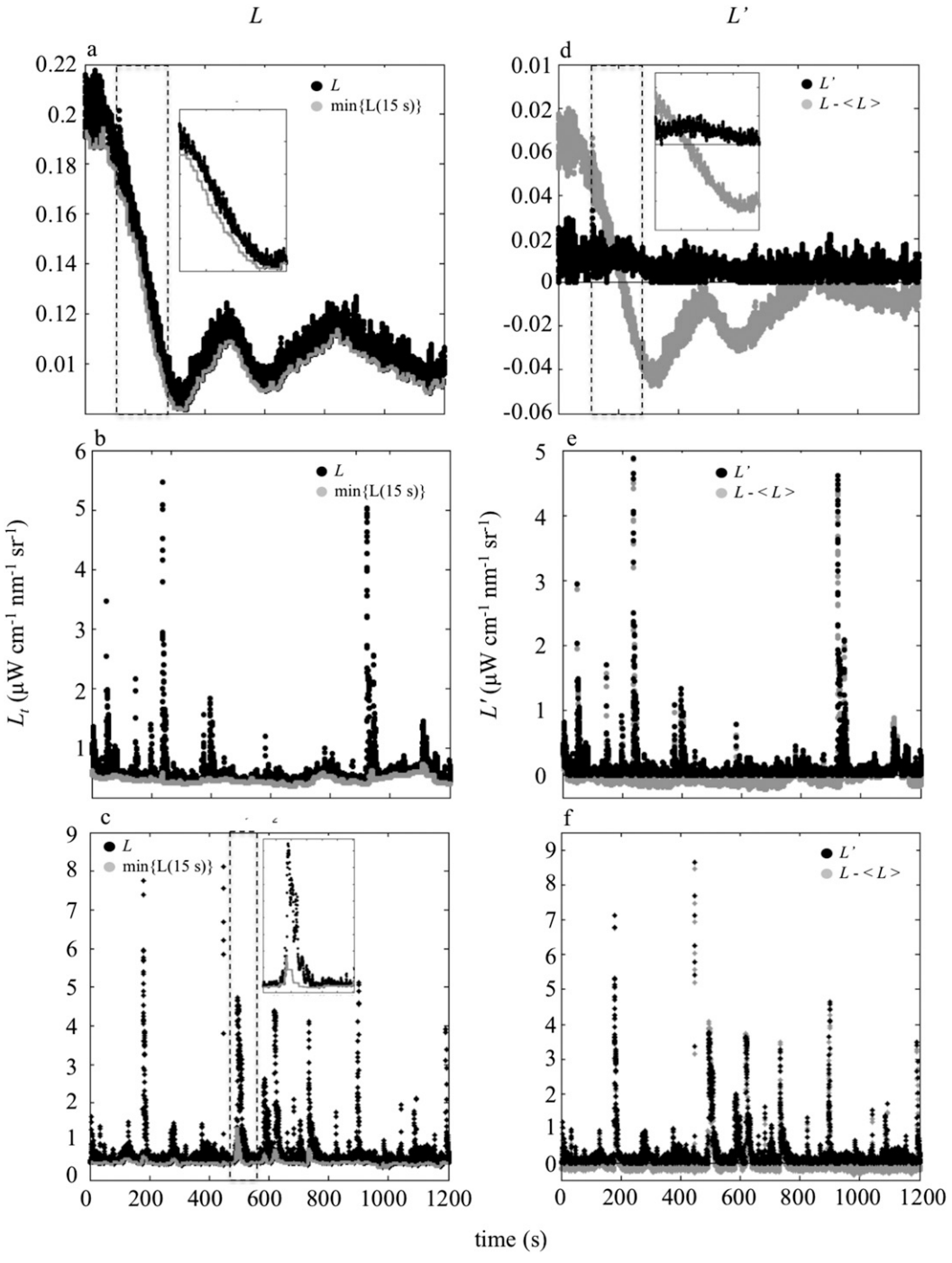

FIG. 7. Short (20 min) records of L_t (black circles) and moving min–max filtered L_t (gray circles) collected under (a) low (day 86, U_{10}~4 m s^{-1}), (b) moderate (day 89, U_{10}~7 m s^{-1}), and (c) high (day 76, U_{10}~10 m s^{-1}) wind conditions; and (d)–(f) the associated L' signals (black circles) shown with the detrended L_t signal for reference. [(a), inset; same axes as in panel] Steep trends in downwelling irradiance (see Fig. 7) are not well captured by the moving min–max filter, [(d), inset; same axes as in panel] resulting in an overestimation of L'. [(c), inset; same axes as in panel] For whitecap events lasting longer than 15 s in duration, the moving min–max filter (15-s window) will erroneously remove a portion of the whitecap feature with the baseline when following the path 1 approach.

Observations in the L_t' or R' record greater than the defined magnitude threshold were identified as whitecap candidates (Fig. 11, pluses). The extent of the IQR (the 25th–75th percentiles identified by the extent of the boxes in Fig. 11b) was determined by the intensity of surface reflected skylight L_r and presented as low-magnitude, high-frequency variance distributed nearly equally across the length of the record (Fig. 12a). The lower detection limit for whitecap samples in the L' or R' record is dependent on the magnitude of L_r. When L_r is large, the lowest magnitude features of the whitecap (e.g., the mature bubble plume) become indiscernible from the background. The remaining nonwhitecap, transient bright features (included as whitecap candidates after applying the magnitude threshold) were removed from the signal using a despiking procedure based on event duration. Bright glintlike features lasting <2 s (14 samples) in duration (easily identified in an L' record, which contains no whitecaps) were eliminated from the pool of whitecap candidates (Fig. 12b).

b. *Results on radiometrically estimated whitecap quantities*

The resulting L'_W and R'_W records were used to calculate a selection of whitecap quantities. For events including stages A and B of the whitecap, quantities describing individual events can be estimated. Decay time and optical intensity were calculated for whitecap events with duration and maximum radiance values above the 75th percentile for the record. For example, *e-folding* time and optical intensity were estimated for short (~12 s) and long (~30 s) breaking events measured during high wind speed (14 m s^{-1}) conditions

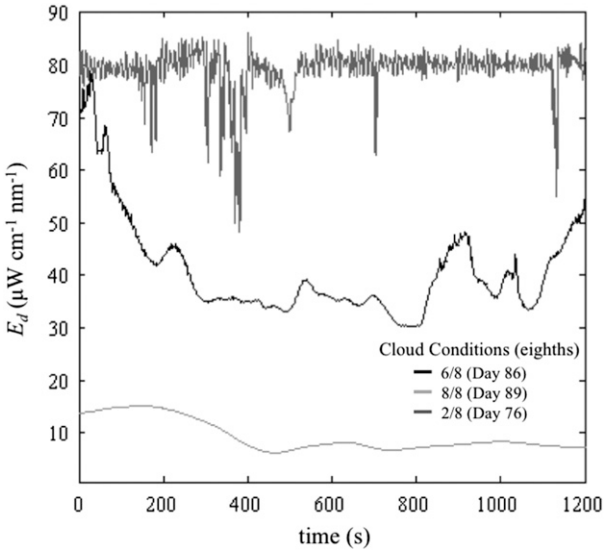

FIG. 8. The E_d measurements corresponding to the L' records for yeardays 86 (black line), 89 (light gray line), and 76 (dark gray line) experiencing low, moderate, and high wind speeds. Cloud conditions, presented in eighths, were 6/8, 8/8 and 2/8, respectively, where 0/8 indicates clear skies and 8/8 indicates overcast. Mostly clear skies on day 76 resulted in an evenly distributed high-frequency, low-magnitude variance throughout the record due to ship motion as the look angle of the detector tilted ~5° into and out of the plane of the sun (dark gray line).

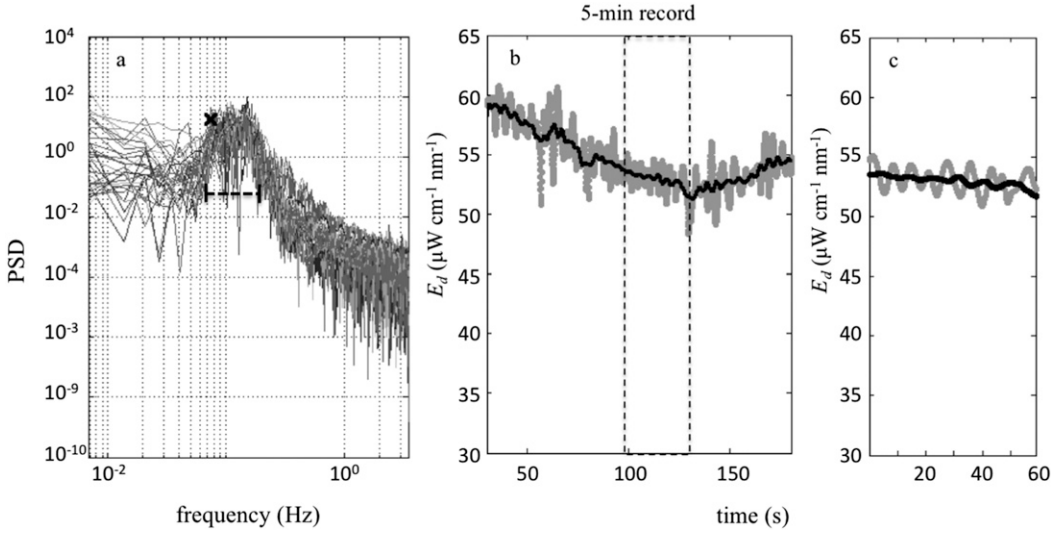

FIG. 9. (a) The peak in the power spectrum of the E_d signal (denoted by the black dotted line), which coincides with the period of the swell, was used to remove the (b),(c) low-magnitude fluctuations in E_d due to slight changes in the look angle as a result of ship motion (gray line), and under nonuniform or clear-sky conditions, the E_d data were filtered using a moving average where the window length was based on the maximum time extent (black line) of the PSD peak [i.e., 14 s; black x symbols in (a)].

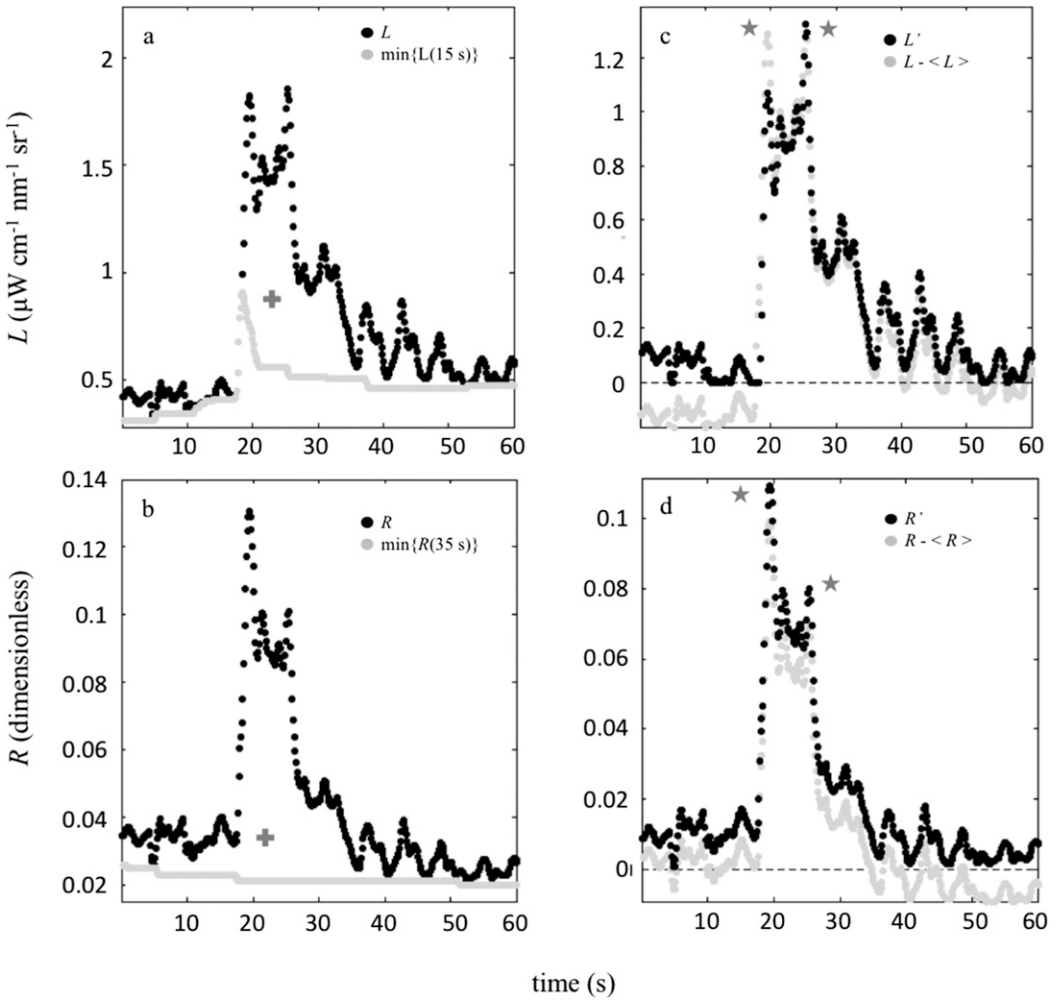

FIG. 10. (a) When applied to a 35-s whitecap feature in L' following path 1 (black circles), the running min-max filter with a 15-s window length produced a baseline (gray circles) that included a portion of the whitecap (gray plus), since local minima occur within the event itself. (b) A 35-s window length applied to the R signal resulted in a baseline that did not erroneously include a portion of the whitecap feature (gray plus). (c),(d) The moving minimum approach offered only an approximation of the ambient illumination conditions (unlike the E_d measurement used in the calculation of R'); therefore, the shapes of the L' and R' signals were similar but not identical (examples indicated with stars).

(Fig. 13). An exponential fit to the binned R'_W data produced an e-folding time of ~4 s for both events, in strong agreement with the 3.53 s reported by Monahan et al. (1982) and the 4.2 s reported by Callaghan et al. (2012). The lower magnitude (R'_{Wmax}~0.36), but longer lasting, event produced an optical intensity of 3.5, while the higher-magnitude (R'_{Wmax}~0.66) short-lived event had an optical intensity of 2.2. The average reflectivities (e.g., approximate albedo) of these breaking events were 20% ($\sigma^2 = 0.16$) and 11% ($\sigma^2 = 0.08$) respectively. The maximum whitecap albedo (LER) for the record ($U_{10\mathrm{N}}$ ~9–15 m s^{-1}) was 68%, exceeding the 55% reflectance of dense foam according to Whitlock et al. (1982) and Stabeno and Monahan (1986). The largest effective reflectance, or mean LER, observed during 9–15 m s^{-1} wind speed conditions was 27%, slightly higher than the 22% effective reflectance of Koepke (1984). On average, however, the effective reflectance measured here was closer to 13%.

Whitecaps identified in the L'_W and R'_W records were also used to calculate the fractional coverage of whitecaps. Substantial scatter exists in the relationship between wind speed and fractional whitecap coverage, primarily because the extent of the sea surface covered by whitecaps at any given time is dependent on many additional factors (marine atmospheric boundary layer stability, wind duration, fetch, sea state, and surfactant

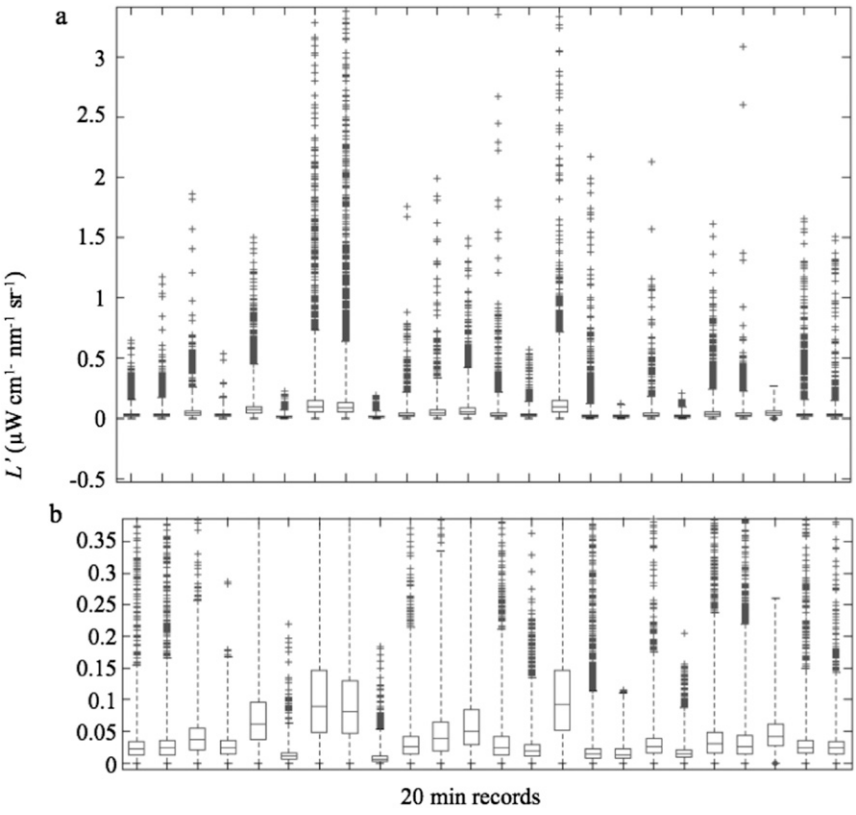

FIG. 11. (a) Boxplot of L' data and (b) an enlargement of the boxes showing the IQR, where the top and bottom of the box represents the 25th and 75 percentiles of L' , respectively, and the center of the box is the median. Whiskers are drawn to 2(IQR) and outliers (indicated by plus symbols) are candidate whitecap samples. The quantity and magnitude of the outliers indicate the frequency of occurrence and the intensity of the whitecaps, respectively.

distribution, etc.) (e.g., Ross and Cardone 1974; Monahan and Monahan 1986; Bortkovskii and Novak 1993; Hanson and Phillips 1999; Zhao and Toba 2001; Stramska and Petelski 2003; Woolf 2005), but also because of uncertainty in W due to undersampling (Callaghan and White 2009).

Coverage estimates were produced using various segment lengths (10–40 min) for stations experiencing different physical forcing conditions (Table 1; Fig. 14, circles). The spatial coverage for each W estimate from the point-based radiometric approach is analogous to spatial coverage per W estimate using digital imaging here (Fig. 14, black squares). Surface drift velocities estimated using atmospheric friction velocities measured in the Southern Ocean were on the order of 10^{-1} m s^{-1}. For an IFOV of ~1 m and an average drift velocity of 0.3 m s^{-1} (i.e., wind friction velocity of ~0.56 m s^{-1}) under 13 m s^{-1} wind speed conditions, a record length of 20 min produces an equivalent area of ~882 m^2. The predicted fractional whitecap coverage under these conditions is ~0.025. To test whether the record length is long enough to provide a good statistical sample, the number of independent events was estimated using the area of individual whitecaps (0.75–2 m^2) from Bondur and Sharkov (1982). For a 13 m s^{-1} wind speed and an individual whitecap area of 1.5 m^2, the number of predicted events is 11. Under similar conditions in the Southern Ocean (i.e., day 76), the radiometric method captured 8–13 independent events, consistent with the number of events predicted.

The fractional coverage of whitecaps estimated for all of SO GasEx by processing 40-min records using the path 1 radiometric method ranged from 0 to 0.043. While a generic 40-min record length was used here to meet the spatial coverage requirement for days with very few whitecaps, it is recommended that record lengths be optimized based on the prevailing physical forcing conditions and system setup, following Eq. (2). Nearly all (87%) of the radiometric coverage estimates were collected within 4 h of those obtained using digital

imagery. However, large changes in whitecap coverage occurring over short time scales made the direct comparison between coverage estimates collected using the different techniques challenging. For example, 160 min of radiometric data were collected on yearday 76, resulting in eight coverage estimates (Fig. 15a). Over a 2-h period during increasing wind forcing (Fig. 15b, blue line), a fourfold increase in whitecap coverage resulted (Fig. 15b, black circles, black line). Four hours earlier on day 76, a fractional coverage of 0.0069 was estimated using digital imagery—an 89% difference relative to the nearest radiometrically derived coverage (Fig. 15b, black square). All radiometric data and digital imagery were collected concomitant with meteorological and oceanographic measurements. However, most of the coverage estimates obtained using the two techniques were not within the same 20-min interval; therefore, the whitecap coverage results were compared using the wind speed–whitecap relationship (Fig. 16).

Coverage estimates obtained using the radiometric (red circles) and digital imaging (gray circles) techniques were compared by binning the data according to the neutral wind speed at 10 m (U_{10N}) in 2 m s^{-1} increments (Table 1; Fig. 16). Although U_{10} has been used to examine the wind speed–whitecap relationship in previously published research, here, in order to account for atmospheric stability, U_{10N} was used. For visualization, whitecap coverage is plotted as $W^{1/3}$; however, we do not assume that all of the wind energy input is dissipated by whitecapping (i.e., large-scale wave breaking; e.g., see Sutherland and Melville 2015). When applying the 2(IQR) threshold, the lowest possible threshold value for the method, the radiometric approach (paths 1 and 2) produced coverage estimates that were consistently statistically significantly higher ($\alpha = 0.05$) than the digital image analysis ($0 \leq p \leq 0.024$), perhaps because it captures more of the whitecap feature, including the spilling crest and the mature bubble plume. For wind speeds of < 6 m s^{-1}, no statistically significant difference was found among the whitecap coverage estimates from the two techniques; however, whitecaps are rarely seen under these wind conditions.

The difference between the coverage estimates was minimized when the magnitude threshold was increased from 2 to 4(IQR) (Fig. 17). The use of a higher threshold with the radiometric data results in the retrieval of strictly the foam features and is comparable to the whitecap coverage measured using the digital imaging technique. As whitecaps mature they become less bright, and the low contrast and the oblique viewing geometry of camera systems deployed to capture a large footprint can result in the omission

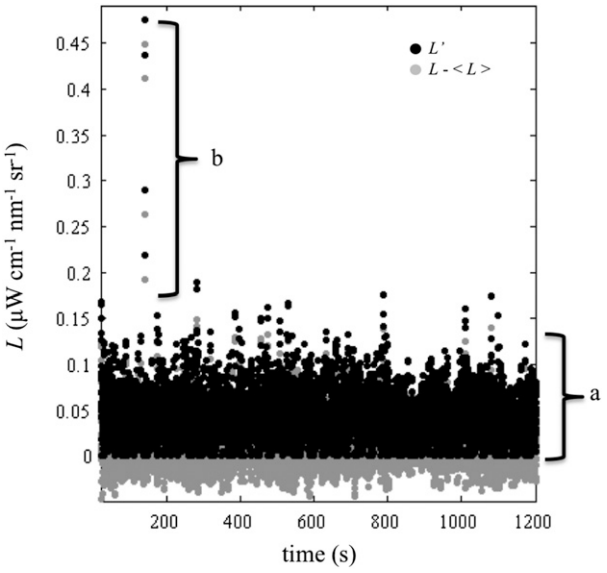

FIG. 12. The detrended (gray circles) total upwelling radiance L_t and baseline removed L_t (L') signals for a low wind speed day (yearday 94, $U_{10} \sim 5.66$ m s^{-1}) with no whitecaps. (a) Most of the variance in the L' signal is attributable to reflected skylight L_r. (b) A bright feature in the L' signal exceeds the magnitude threshold requirement identifying whitecaps, but it is removed from the pool of whitecap candidates in the duration filter.

of a portion of the whitecap, producing a lower estimate of W (Stramska and Petelski 2003; Anguelova and Webster 2006).

The optimal fit of the radiometrically estimated whitecap coverage (path 1) to the neutral wind speed at 10 m was determined using robust linear least squares. Whitecap coverage showed a near-cubic dependence on wind speed (Fig. 18, black line) when the 2(IQR) threshold was used to capture the full whitecap feature. When the difference between whitecap coverage measured radiometrically (Fig. 18, black dashed line) and using the digital imaging technique (Fig. 18, gray line) is minimized [i.e., 4(IQR)], the whitecap coverage estimate captures ~50%–85% of the total whitecap feature obtained using the 2(IQR) threshold.

c. *Comparison to previously published whitecap coverage measurements*

Several previously published, widely recognized wind speed–whitecap relationships are included for comparison. A more complete review of the empirical relationships between whitecap coverage and wind speed can be found in Goddijn-Murphy et al. (2011) and Scanlon and Ward (2016). The radiometric parameterization using the 4(IQR) threshold is most comparable to the Monahan and Muircheartaigh (1980) parameterization using robust

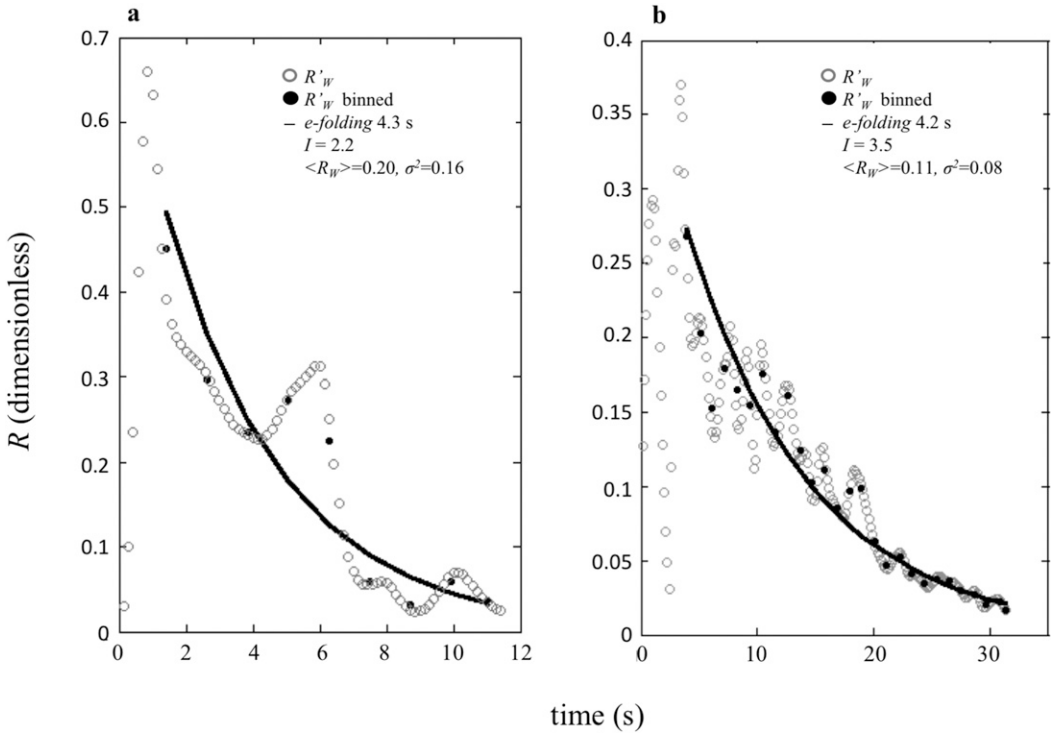

FIG. 13. (a) An exponential fit to the binned R'_W data from a short (~12 s) breaking event measured during high wind speed conditions (14 m s^{-1}) produced an *e*-folding time of 4.3 s, an optical intensity$I$ of 2.2, and an average reflectivity of 0.20 ($\sigma^2 = 0.16$). (b) The lower-magnitude (R'_{Wmax} of ~0.36) but longer-lasting (~30 s) breaking event produced an *e*-folding time of 4.2 s, an optical intensity of 3.5, and an average reflectivity of 0.11 ($\sigma^2 = 0.08$).

biweight fitting to data collected in the Atlantic and Pacific Oceans ($M80_{RBF}$; Fig. 18b, green line) (0%–17% difference). The radiometric approach produces lower estimates of fractional whitecap coverage for wind speeds $< 12\,\mathrm{m\,s^{-1}}$, perhaps due to undersampling under high wind conditions. During SO GasEx, no data were collected for wind speeds exceeding $14\,\mathrm{m\,s^{-1}}$. The Stramska and Petelski (2003) (SP_{DEV}; Fig. 18, blue line) parameterization for developed seas using data from the North Atlantic Ocean produces substantially lower estimates of W for wind speeds $< 10\,\mathrm{m\,s^{-1}}$ [7%–150% lower than 4(IQR)] and then 17%–45% higher estimates for $U_{10} > 12\,\mathrm{m\,s^{-1}}$. Additional parameterizations, including the historical stage A and stage B fractional coverage by Monahan (1993), and those by Asher and Wanninkhof (1998) (cyan line), Hanson and Phillips (1999) (red line), and Villarino et al. (2003) (pink line) are also included (Fig. 18b).

d. Limitations of the radiometric approach

The radiometric approach is conservative in its design to minimize the risk of producing false positive errors in the estimates of whitecap quantities. As a result, the threshold [i.e., 2(IQR)] and the added duration filter (i.e., >2 s) could result in the exclusion of the final portion of the mature or decaying bubble plume and of any foam streak or spume line features present. Also, certain environmental conditions result in the loss of

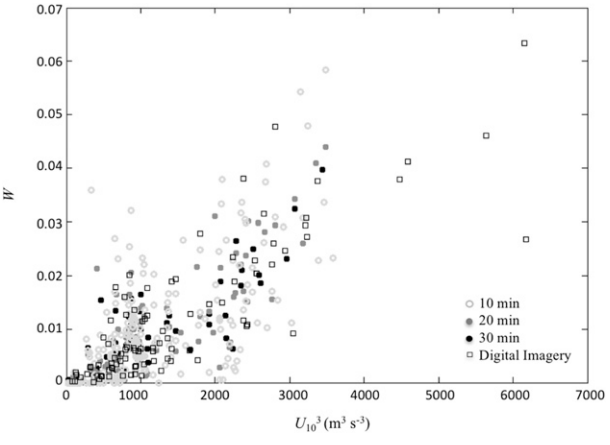

FIG. 14. Whitecap coverage from radiometric data as a function of cubic wind speed using 10-min (open circles), 20-min (gray circles), and 30-min (black circles) record lengths based on a 4(IQR) threshold for direct comparison to the 20-min fractional whitecap coverage estimates obtained using digital imagery.

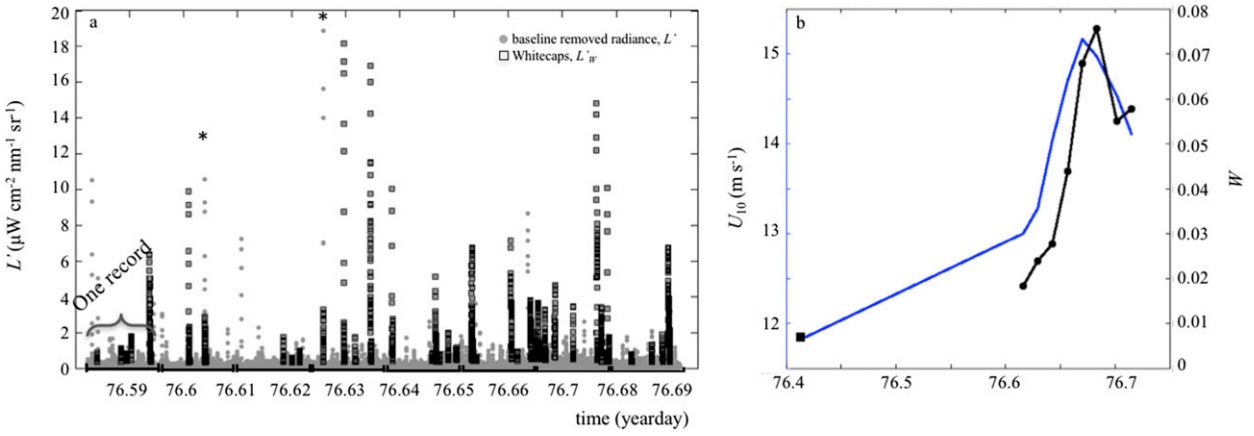

FIG. 15. (a) Whitecap coverage estimates were determined from whitecap samples (black squares) identified in eight 20-min records (black lines along the *x*-axis differentiate the eight segments) of L' from day 76 (gray circles) following the path 1 approach. (b) The trend in radiometrically estimated whitecap coverage (black circles and line) closely followed the wind speed record (blue line) over the 2-h period of sampling. Four hours earlier on day 76, a fractional coverage of 0.0069 was estimated using digital imagery (black square), an 89% difference relative to the nearest radiometrically derived coverage.

some whitecap features or preclude the use of the radiometric method altogether. Surface-reflected skylight determines the detection limit for whitecaps. When L_r is large, the darker, lower-magnitude whitecap features (i.e., the mature bubble plume) cannot be differentiated from surface-reflected skylight. Under such conditions, the mature bubble plume is excluded from the whitecap retrieval when using either the path 1 or path 2 approach. Although not seen here, strong trends in downwelling irradiance that are not effectively captured following path 1 could, in extreme cases, result in false positive whitecap identification. Under such conditions, the path 2 approach is recommended. The radiometric technique is not recommended for use under erratic downwelling irradiance conditions (i.e., spikey E_d signal) when the E_d sensor is not gimbaled. Under such conditions, the path 1 approach would not effectively capture the changing illumination conditions in the baseline estimation, producing false-positive whitecap identifications. Similarly, the filtering necessary to correct the downwelling irradiance data for ship motion using the path 2 approach (i.e., moving average with a window length based on the period of the swell)

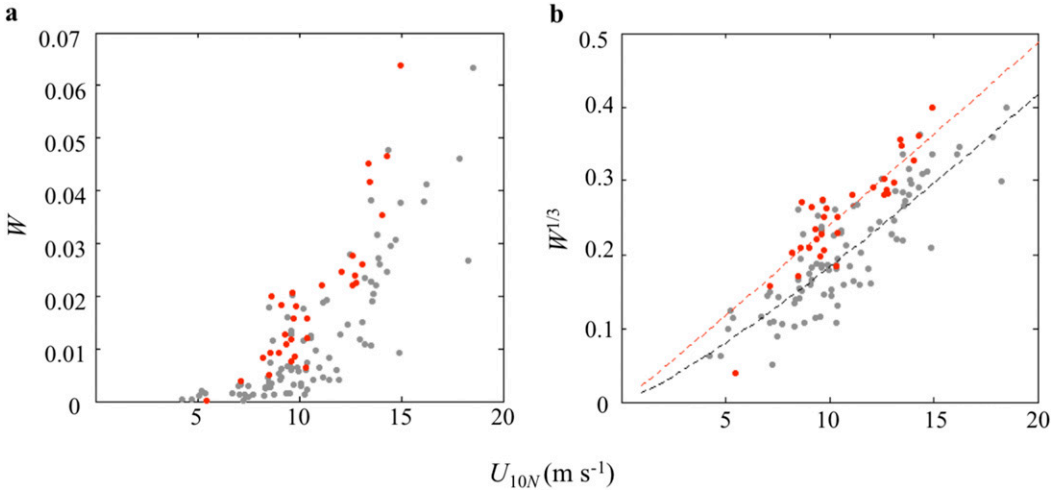

FIG. 16. (a) Whitecap coverage estimated using the path 1 approach with a 2(IQR) magnitude threshold (red circles), the lowest possible threshold value for the method, and the digital imaging approach (gray circles) as a function of the neutral wind speed at 10 m. (b) The red and gray dashed lines correspond to the linear least squares fit to the radiometrically and videographically derived whitecap coverages, respectively.

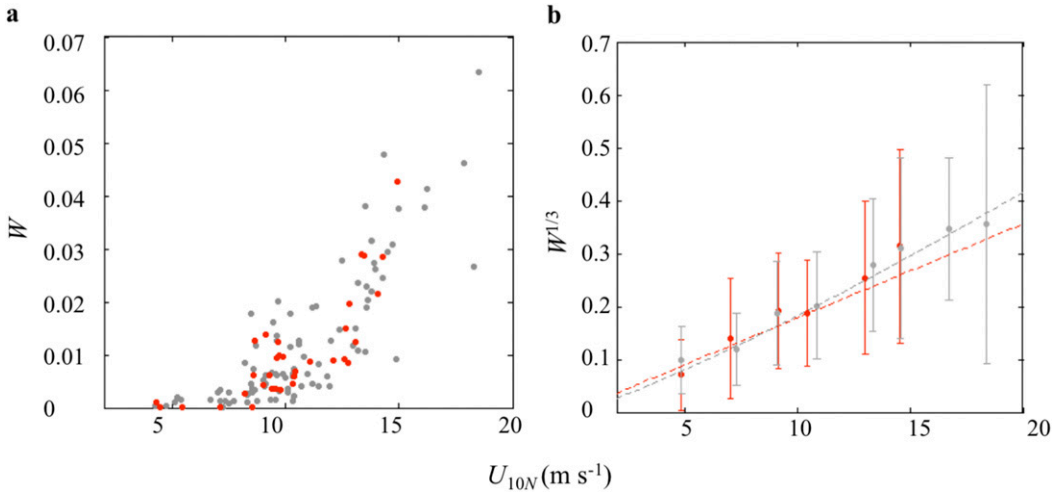

FIG. 17. (a) Whitecap coverage estimated using the path 1 approach with a 4(IQR) magnitude threshold (red circles and standard error) that includes only the bright foam features in the estimation of W and the fractional coverage obtained using digital imagery (gray circles and standard error) as a function of the neutral wind speed at 10 m. (b) The dashed red and gray lines are the least squares fit to whitecap coverage estimated using the radiometric and digital imaging approaches, respectively.

will not preserve fleeting spikes in E_d, resulting in erroneous R' values.

6. Conclusions

Whitecap quantities (e.g., fractional coverage, optical intensity, decay time, and albedo) are easily obtainable using the simple, efficient, automated, and robust radiometric measurement described here. The method is flexible and objective; the field of view, the height of the instrument above the waterline, and the speed over ground (in the case of a moving vessel) can be tuned to optimize the measurement of the whitecap quantity of interest. Furthermore, the nature of the measurement likely allows more of the decaying whitecap feature, including the surface manifestation of the γ plume, to be measured compared to the digital imaging approach. Capturing the mature portion of the whitecap (i.e., bubble plume) has implications for gas transfer, specifically for lower solubility gases (e.g., Woolf and Thorpe 1991), and the production of primary marine sea salt aerosols (e.g., Monahan et al. 1986). When only the bright, foam features are included in the radiometric estimation of W [e.g., 4(IQR) threshold], strong agreement was found with coverage measured concurrently using digital imagery collected in the Southern Ocean. Also, when the high threshold is used and the mature whitecap features are excluded from the whitecap coverage estimate [e.g., 4(IQR) threshold], strong agreement can be found between the radiometrically derived and previously published wind speed–whitecap parameterizations. While whitecap coverage estimates using the radiometric and digital imaging techniques were compared here using the wind speed–whitecap relationship, efforts should be made to provide direct comparisons between whitecap features measured using the two approaches.

The use of ocean color radiometers with high sensitivity in a greater number of narrow spectral bands can allow for a comprehensive analysis of whitecap features. The effect of whitecaps on the spectral shape of visible light leaving the ocean surface has been reported in previously published studies (e.g., Koepke 1984; Frouin et al. 1996; Moore et al. 2000; Stramski and Tegowski 2001; Zhang et al. 2002) and using the dataset presented here (Randolph 2015). Applying intensity intervals representative of each stage of the whitecap (e.g., Donelan et al. 1972; Bondur and Sharkov 1982; Stabeno and Monahan 1986; Bortkovskii 1987; Monahan 1989; Callaghan et al. 2012) and changes in the spectral shape within a small instantaneous field of view can allow for whitecap features to be parsed into stages (e.g., A and the α plume, B and the β plume and, finally, the γ plume). Furthermore, measurements of ocean color can be used to estimate the in-water constituents [e.g., chromophoric dissolved organic matter (CDOM), surfactants, phytoplankton concentration, and composition] affecting the evolution of foam and bubbles, which has implications for air–sea exchange processes. Ultimately, because the system is adaptable and inexpensive in terms of processing time, application of the radiometric method can supply more data in support of investigations into the evolution and role of whitecaps.

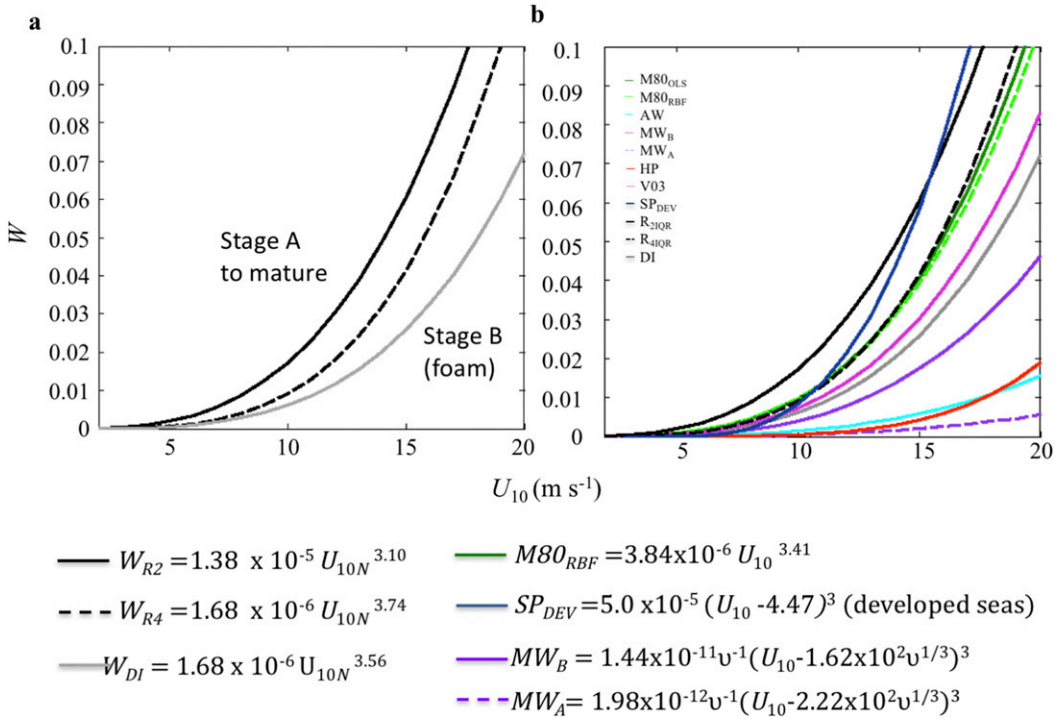

FIG. 18. (a) The relationship between wind speed (U_{10N}) and W obtained using the radiometric method with the 2(IQR) (R_{2IQR}) and 4(IQR) (R_{4IQR}) thresholds and whitecap coverage obtained using digital imagery (DI, gray line) were estimated using linear least squares (solid and dashed black lines, respectively). (b) Previously published wind speed–whitecap parameterizations (based on the instantaneous wind speed at 10 m), including Monahan and Muircheartaigh (1980) (M80$_{RBF}$, green line), Stramska and Petelski (2003) using data from developed seas (SP$_{DEV}$; blue line), and Monahan (1993) using a combination of historical datasets, including stage A (MW$_A$, pink line) and stage B (MW$_B$, purple line) whitecaps are shown for comparison. Additional parameterizations, including those published by Asher and Wanninkhof (1998) (cyan line), Hanson and Phillips (1999) (red line), and Villarino et al. (2003) (pink line) are also included.

Acknowledgments. This research was supported by NASA's Ocean Biology and Biogeochemistry Program (NNX08AB10G, Dierssen). Additional support was also provided by NOAA (NA07OAR4310094, Zappa) and NSF (0647667, Zappa). We thank Scott Freeman and Christopher Buonassissi for the collection of optical data. We thank James Edson for his advice and the collection and processing of the meteorological data, and Michael Twardowski for providing suggestions that substantially strengthened this paper. Finally, we thank Brian Ward and Brian Scanlon and two anonymous reviewers for providing comments that significantly improved the clarity of the ideas presented.

REFERENCES

Andreas, E. L, J. B. Edson, E. C. Monahan, M. P. Rouault, and S. D. Smith, 1995: The spray contribution to net evaporation from the sea: A review of recent progress. *Bound.-Layer Meteor.*, **72**, 3–52, doi:10.1007/BF00712389.

Anguelova, M. D., and F. Webster, 2006: Whitecap coverage from satellite measurements: A first step toward modeling the variability of oceanic whitecaps. *J. Geophys. Res.*, **111**, C03017, doi:10.1029/2005JC003158.

Asher, W. E., and R. Wanninkhof, 1998: The effect of bubble-mediated gas transfer on purposeful dual-gaseous tracer experiments. *J. Geophys. Res.*, **103**, 10 555–10 560, doi:10.1029/98JC00245.

——, L. M. Karle, B. J. Higgins, P. J. Farley, I. S. Leifer, and E. C. Monahan, 1995: The effect of bubble plume size on the parameterization of air-seawater gas transfer velocities. *Air-Water Gas Transfer: Selected Papers from the Third International Symposium on Air-Water Gas Transfer*, B. Jähne and E. C. Monahan, Eds., AEON-Verlag and Studio, 227–238.

——, J. Edson, W. McGillis, R. Wanninkhof, D. T. Ho, and T. Litchendorf, 2002: Fractional area whitecap coverage and air-sea gas transfer velocities measured during GasEx-98. *Gas Transfer at Water Surfaces*, *Geophys. Monogr.*, Vol. 127, Amer. Geophys. Union, 199–203.

Balch, W. M., D. T. Drapeau, B. C. Bowler, E. Lyczskowski, E. S. Booth, and D. Alley, 2011: The contribution of coccolithophores to the optical and inorganic carbon budgets during the Southern Ocean Gas Exchange Experiment: New evidence in support of the "Great Calcite Belt" hypothesis. *J. Geophys. Res.*, **116**, C00F06, doi:10.1029/2011JC006941.

Bondur, V. G., and E. A. Sharkov, 1982: Statistical properties of whitecaps on a rough sea. *Oceanology*, **22**, 274–279.

Bortkovskii, R. S., 1987: *Air-Sea Exchange of Heat and Moisture during Storms*. Atmospheric Sciences Library, Vol. 10, Kluwer, 194 pp., doi:10.1007/978-94-017-0687-2.

——, and V. Novak, 1993: Statistical dependencies of sea state characteristics on water temperature and wind-wave age. *J. Mar. Syst.*, **4**, 161–169, doi:10.1016/0924-7963(93)90006-8.

Bouguet, J.-Y., 2004: Camera calibration toolbox for MATLAB. Microprocessor Research Laboratory, Intel Corp. [Available online at http://www.vision.caltech.edu/bouguetj/calib_doc/.]

Briggs, N., M. J. Perry, I. Cetinić, C. Lee, E. D'Asaro, A. M. Gray, and E. Rehm, 2011: High-resolution observations of aggregate flux during a sub-polar North Atlantic spring bloom. *Deep-Sea Res. I*, **58**, 1031–1039, doi:10.1016/j.dsr.2011.07.007.

Callaghan, A. H., and M. White, 2009: Automated processing of sea surface images for the determination of whitecap coverage. *J. Atmos. Oceanic Technol.*, **26**, 383–394, doi:10.1175/2008JTECHO634.1.

——, G. B. Deane, M. D. Stokes, and B. Ward, 2012: Observed variation in the decay time of oceanic whitecap foam. *J. Geophys. Res.*, **117**, C09015, doi:10.1029/2012JC008147.

Cifuentes-Lorenzen, A., J. B. Edson, C. J. Zappa, and L. Bariteau, 2013: A multisensor comparison of ocean wave frequency spectra from a research vessel during the Southern Ocean Gas Exchange Experiment. *J. Atmos. Oceanic Technol.*, **30**, 2907–2925, doi:10.1175/JTECH-D-12-00181.1.

Donelan, M., M. S. Longuet-Higgins, and J. S. Turner, 1972: Periodicity in whitecaps. *Nature*, **239**, 449–451, doi:10.1038/239449a0.

Drennan, W. M., M. Donelan, E. Terray, and K. Katsaros, 1996: Oceanic turbulence dissipation measurements in SWADE. *J. Phys. Oceanogr.*, **26**, 808–815, doi:10.1175/1520-0485(1996)026<0808:OTDMIS>2.0.CO;2.

Edson, J. B., and C. Fairall, 1998: Similarity relationships in the marine atmospheric surface layer for terms in the TKE and scalar variance budgets. *J. Atmos. Sci.*, **55**, 2311–2328, doi:10.1175/1520-0469(1998)055<2311:SRITMA>2.0.CO;2.

——, and Coauthors, 2011: Direct covariance measurement of CO_2 gas transfer velocity during the 2008 Southern Ocean Gas Exchange Experiment: Wind speed dependency. *J. Geophys. Res.*, **116**, C00F10, doi:10.1029/2011JC007022.

Fairall, C. W., E. F. Bradley, J. E. Hare, A. A. Grachev, and J. B. Edson, 2003: Bulk parameterization of air–sea fluxes: Updates and verification for the COARE algorithm. *J. Climate*, **16**, 571–591, doi:10.1175/1520-0442(2003)016<0571:BPOASF>2.0.CO;2.

Frouin, R., M. Schwindling, and P.-Y. Deschamps, 1996: Spectral reflectance of sea foam in the visible and near-infrared: In situ measurements and remote sensing implications. *J. Geophys. Res.*, **101**, 14 361–14 371, doi:10.1029/96JC00629.

Gemmrich, J. R., and D. M. Farmer, 1999: Observations of the scale and occurrence of breaking surface waves. *J. Phys. Oceanogr.*, **29**, 2595–2606, doi:10.1175/1520-0485(1999)029<2595:OOTSAO>2.0.CO;2.

——, M. L. Banner, and C. Garrett, 2008: Spectrally resolved energy dissipation rate and momentum flux of breaking waves. *J. Phys. Oceanogr.*, **38**, 1296–1312, doi:10.1175/2007JPO3762.1.

Goddijn-Murphy, L., D. K. Woolf, and A. H. Callaghan, 2011: Parameterizations and algorithms for oceanic whitecap coverage. *J. Phys. Oceanogr.*, **41**, 742–756, doi:10.1175/2010JPO4533.1.

Hanson, J. L., and O. M. Phillips, 1999: Wind sea growth and dissipation in the open ocean. *J. Phys. Oceanogr.*, **29**, 1633–1648, doi:10.1175/1520-0485(1999)029<1633:WSGADI>2.0.CO;2.

Ho, D. T., and Coauthors, 2011: Southern Ocean Gas Exchange Experiment: Setting the stage. *J. Geophys. Res.*, **116**, C00F08, doi:10.1029/2010JC006852.

Kleiss, J. M., and W. K. Melville, 2011: The analysis of sea surface imagery for whitecap kinematics. *J. Atmos. Oceanic Technol.*, **28**, 219–243, doi:10.1175/2010JTECHO744.1.

Koepke, P., 1984: Effective reflectance of oceanic whitecaps. *Appl. Opt.*, **23**, 1816–1824, doi:10.1364/AO.23.001816.

Kudryavtsev, V., and V. Makin, 2002: Coupled dynamics of short waves and the airflow over long surface waves. *J. Geophys. Res.*, **107**, 3209, doi:10.1029/2001JC001251.

Lemire, D., 2006: Streaming maximum-minimum filter using no more than three comparisons per element. *Nord. J. Comput.*, **13**, 328–339.

Liss, P. S., and L. Merlivat, 1986: Air-sea gas exchange rates: Introduction and synthesis. *The Role of Air-Sea Exchange in Geochemical Cycling*, P. Buat-Ménard, Ed., NATO Science Series C, Vol. 185, D. Reidel, 113–129.

Mobley, C. D., 1999: Estimation of the remote-sensing reflectance from above-surface measurements. *Appl. Opt.*, **38**, 7442–7455, doi:10.1364/AO.38.007442.

Monahan, E. C., 1989: From the laboratory tank to the global ocean. *The Climate and Health Implications of Bubble-Mediated Sea-Air Exchange*, Connecticut Sea Grant College Program, 43–63.

——, 1993: Occurrence and evolution of acoustically relevant subsurface bubble plumes and their associated, remotely monitorable, surface whitecaps. *Natural Physical Sources of Underwater Sound: Sea Surface Sound (2)*, B. R. Kerman, Ed., Springer, 503–517.

——, 2002: Oceanic whitecaps: Sea surface features detectable via satellite that are indicators of the magnitude of the air-sea gas transfer coefficient. *J. Earth Syst. Sci.*, **111**, 315–319, doi:10.1007/BF02701977.

——, and C. R. Zietlow, 1969: Laboratory comparisons of freshwater and salt-water whitecaps. *J. Geophys. Res.*, **74**, 6961–6966, doi:10.1029/JC074i028p06961.

——, and I. O. Muircheartaigh, 1980: Optimal power-law description of oceanic whitecap coverage dependence on wind speed. *J. Phys. Oceanogr.*, **10**, 2094–2099, doi:10.1175/1520-0485(1980)010<2094:OPLDOO>2.0.CO;2.

——, and M. C. Spillane, 1984: The role of oceanic whitecaps in air sea gas exchange. *Gas Transfer at Water Surfaces*, W. Brutsaert and G. H. Jirka, Eds., Water Science and Technology Library, Vol. 2, D. Reidel, 495–504.

——, and C. F. Monahan, 1986: The influence of fetch on whitecap coverage as deduced from the Alte Weser Light-station observer's log. *Oceanic Whitecaps: And Their Role in Air–Sea Exchange Processes*, E. Monahan and G. M. Niocaill, Eds., Oceanographic Sciences Library, Vol. 2, D. Reidel, 275–277.

——, and M. Lu, 1990: Acoustically relevant bubble assemblages and their dependence on meteorological parameters. *IEEE J. Oceanic Eng.*, **15**, 340–349, doi:10.1109/48.103530.

Monahan, E., K. Davidson, and D. Spiel, 1982: Whitecap aerosol productivity deduced from simulation tank measurements. *J. Geophys. Res.*, **87**, 8898–8904, doi:10.1029/JC087iC11p08898.

——, M. C. Spillane, P. A. Bowyer, M. R. Higgins, and P. J. Stabeno, 1984: Whitecaps and the marine atmosphere. University College Tech. Rep. 7, 103 pp. [Available online at https://aran.library.nuigalway.ie/handle/10379/4263.]

——, D. E. Spiel, and K. L. Davidson, 1986: A model of marine aerosol generation via whitecaps and wave disruption. *Oceanic Whitecaps: And Their Role in Air–Sea Exchange Processes*, E. Monahan and G. M. Niocaill, Eds., Oceanographic Sciences Library, Vol. 2, D. Reidel, 167–174.

Moore, K. D., K. J. Voss, and H. R. Gordon, 1998: Spectral reflectance of whitecaps: Instrumentation, calibration, and performance in coastal waters. *J. Atmos. Oceanic Technol.*, **15**, 496–509, doi:10.1175/1520-0426(1998)015<0496:SROWIC>2.0.CO;2.

——, ——, and ——, 2000: Spectral reflectance of whitecaps: Their contribution to water-leaving radiance. *J. Geophys. Res.*, **105**, 6493–6499, doi:10.1029/1999JC900334.

Mueller, J. L., and Coauthors, 2003: Radiometric measurements and data analysis protocols. Vol. III, Ocean optics protocols for satellite ocean color sensor validation, revision 4, J. L. Mueller, G. S. Fargion, and C. R. McClain, Eds., NASA Tech. Memo. NASA/TM-2003-21621/Rev-VolIII, 78 pp. [Available online at https://oceancolor.gsfc.nasa.gov/DOCS/Protocols_Ver4_VolIII.pdf.]

Nordberg, W., J. Conaway, D. B. Ross, and T. Wilheit, 1971: Measurements of microwave emission from a foam-covered, wind-driven sea. *J. Atmos. Sci.*, **28**, 429–435, doi:10.1175/1520-0469(1971)028<0429:MOMEFA>2.0.CO;2.

Randolph, K. L., 2015: Optical measurements of whitecaps and bubbles during large scale wave breaking in the Southern Ocean. Ph.D. dissertation, University of Connecticut, 146 pp.

——, H. M. Dierssen, M. Twardowski, A. Cifuentes-Lorenzen, and C. J. Zappa, 2014: Optical measurements of small deeply penetrating bubble populations generated by breaking waves in the Southern Ocean. *J. Geophys. Res. Oceans*, **119**, 757–776, doi:10.1002/2013JC009227.

Ross, D. B., and V. Cardone, 1974: Observations of oceanic whitecaps and their relation to remote measurements of surface wind speed. *J. Geophys. Res.*, **79**, 444–452, doi:10.1029/JC079i003p00444.

Scanlon, B., and B. Ward, 2016: The influence of environmental parameters on active and maturing oceanic whitecaps. *J. Geophys. Res. Oceans*, **121**, 3325–3336, doi:10.1002/2015JC011230.

——, Ø. Breivik, J.-R. Bidlot, P. A. Janssen, A. H. Callaghan, and B. Ward, 2016: Modeling whitecap fraction with a wave model. *J. Phys. Oceanogr.*, **46**, 887–894, doi:10.1175/JPO-D-15-0158.1.

Stabeno, P. J., and E. C. Monahan, 1986: The influence of whitecaps on the albedo of the sea surface. *Oceanic Whitecaps: Their Role in Air-Sea Exchange Processes*, E. C. Monahan and G. M. Niocaill, Eds., Oceanographic Sciences Library, Vol. 2, D. Reidel, 261–266.

Stramska, M., and T. Petelski, 2003: Observations of oceanic whitecaps in the north polar waters of the Atlantic. *J. Geophys. Res.*, **108**, 3086, doi:10.1029/2002JC001321.

Stramski, D., and J. Tegowski, 2001: Effects of intermittent entrainment of air bubbles by breaking wind waves on ocean reflectance and underwater light field. *J. Geophys. Res.*, **106**, 31 345–31 360, doi:10.1029/2000JC000461.

Sugihara, Y., H. Tsumori, T. Ohga, H. Yoshioka, and S. Serizawa, 2007: Variation of whitecap coverage with wave-field conditions. *J. Mar. Syst.*, **66**, 47–60, doi:10.1016/j.jmarsys.2006.01.014.

Sutherland, P., and W. K. Melville, 2015: Field measurements of surface and near-surface turbulence in the presence of breaking waves. *J. Phys. Oceanogr.*, **45**, 943–965, doi:10.1175/JPO-D-14-0133.1.

Terray, E., M. Donelan, Y. Agrawal, W. Drennan, K. Kahma, A. Williams, P. Hwang, and S. Kitaigorodskii, 1996: Estimates of kinetic energy dissipation under breaking waves. *J. Phys. Oceanogr.*, **26**, 792–807, doi:10.1175/1520-0485(1996)026<0792:EOKEDU>2.0.CO;2.

Terrill, E. J., W. K. Melville, and D. Stramski, 2001: Bubble entrainment by breaking waves and their influence on optical scattering in the upper ocean. *J. Geophys. Res.*, **106**, 16 815–16 823, doi:10.1029/2000JC000496.

Thorpe, S. A., 1982: On the clouds of bubbles formed by breaking wind-waves in deep water, and their role in air–sea gas transfer. *Philos. Trans. Roy. Soc. London*, **304A**, 155–210, doi:10.1098/rsta.1982.0011.

Villarino, R., A. Camps, M. Vall-Ilossera, J. Miranda, and J. Arenas, 2003: Sea foam effects on the brightness temperature at L-band. *IGARSS 2003: 2003 IEEE International Geoscience and Remote Sensing Symposium; Proceedings*, Vol. 5, IEEE, 3076–3078, doi:10.1109/IGARSS.2003.1294688.

Wang, Q., E. C. Monahan, W. E. Asher, and P. M. Smith, 1995: Correlations of whitecap coverage and gas transfer velocity with microwave brightness temperature for plunging and spilling breaking waves. *Air-Water Gas Transfer: Selected Papers from the Third International Symposium on Air-Water Gas Transfer*, B. Jähne and E. C. Monahan, Eds., AEON-Verlag and Studio, 217–225.

Whitlock, C. H., D. S. Bartlett, and E. A. Gurganus, 1982: Sea foam reflectance and influence on optimum wavelength for remote sensing of ocean aerosols. *Geophys. Res. Lett.*, **9**, 719–722, doi:10.1029/GL009i006p00719.

Woolf, D. K., 2005: Parametrization of gas transfer velocities and sea-state-dependent wave breaking. *Tellus*, **57B**, 87–94, doi:10.1111/j.1600-0889.2005.00139.x.

——, and S. A. Thorpe, 1991: Bubbles and the air-sea exchange of gases in near-saturation conditions. *J. Mar. Res.*, **49**, 435–466, doi:10.1357/002224091784995765.

Wu, J., 1983: Sea-surface drift currents induced by wind and waves. *J. Phys. Oceanogr.*, **13**, 1441–1451, doi:10.1175/1520-0485(1983)013<1441:SSDCIB>2.0.CO;2.

Zappa, C. J., M. L. Banner, H. Schultz, J. R. Gemmrich, R. P. Morison, D. A. LeBel, and T. Dickey, 2012: An overview of sea state conditions and air-sea fluxes during RaDyO. *J. Geophys. Res.*, **117**, C00H19, doi:10.1029/2011JC007336.

Zhang, X., M. Lewis, M. Lee, B. Johnson, and G. Korotaev, 2002: The volume scattering function of natural bubble populations. *Limnol. Oceanogr.*, **47**, 1273–1282, doi:10.4319/lo.2002.47.5.1273.

Zhao, D., and Y. Toba, 2001: Dependence of whitecap coverage on wind and wind-wave properties. *J. Oceanogr.*, **57**, 603–616, doi:10.1023/A:1021215904955.

Zibordi, G., and C. J. Donlon, 2014: In situ measurement strategies. *Optical Radiometry for Ocean Climate Measurements*, G. Zibordi, C. J. Donlon, and A. C. Parr, Eds., Experimental Methods in the Physical Sciences, Vol. 47, Elsevier, 527–529.